Title
Leveraging Aberrant Iron Metabolism as a Method for Selective Drug Delivery and Imaging In Vivo

Author
Muir, Ryan Keith

Publication Date
2019

Peer reviewed|Thesis/dissertation

Leveraging Aberrant Iron Metabolism as a Method for Selective Drug Delivery and Imaging In Vivo

by

Ryan Muir

DISSERTATION

Submitted in partial satisfaction of the requirements for degree of

DOCTOR OF PHILOSOPHY

in

Chemistry and Chemical Biology

in the

GRADUATE DIVISION

of the

UNIVERSITY OF CALIFORNIA, SAN FRANCISCO

Approved:

DocuSigned by:

Adam Renslo

FBDB6299FCD244B...

Adam Renslo

Chair

DocuSigned by:

Jason Gestwicki

Jason Gestwicki

DocuSigned by:

Jim Wells

Jim Wells

DocuSigned by:

Davide Ruggero

14C3B6AD60C5446...

Davide Ruggero

Committee Members

Dedications and Acknowledgements

I would like to thank everybody who has helped me get to this point in my life, both scientifically and personally. First, I need to thank my parents for being unconditionally supportive of whatever I want to pursue. I'd like to thank my family and friends for providing a great support network through the ups and downs of graduate school. I'd like to thank Dr. Adam Renslo for being a phenomenal boss and mentor. I'd also like to thank everybody in the Renslo lab that has helped me so much throughout my time at UCSF, with special thanks to Dr. Brian Blank for his chemistry mentoring. Lastly, I'd like to thank my partner Tia Tummino for the years of support both scientifically and personally. Everybody listed above have been tremendously helpful on this journey, and I am deeply appreciative.

Contributions

Chapter 2 is adapted from Muir, R. K., Zhao, N., Wei, J., Wang, Y. H., Moroz, A., Huang, Y., Chen, Y.C., Sriram, R., Kurhanewicz, J., Ruggero, D., Renslo, A.R., Evans, M. J. (2019). Measuring Dynamic Changes in the Labile Iron Pool in Vivo with a Reactivity-Based Probe for Positron Emission Tomography. *ACS central science*, *5*(4), 727–736. doi:10.1021/acscentsci.9b00240

Leveraging Aberrant Iron Metabolism as a Method for Selective Drug Delivery and Imaging In Vivo

Ryan Muir

Abstract

Iron is a nutrient essential for cell growth and proliferation, however too high of a concentration can cause the formation of toxic reactive oxygen species. As a result, normal cells tightly regulate iron metabolism. Many cancers have been noted to possess aberrant expression of various proteins in the iron metabolism pathway, with a strong correlation between a higher avidity for iron and worse patient prognosis. Recently the Renslo lab has sought to leverage this elevated level of iron utilizing an Fe(II)-activated prodrug platform based on the reactivity of 1,2,4-trioxolanes (TRX). Previous studies have demonstrated selective delivery of amine-bearing cytotoxins to cancers with elevated Fe(II) pools. Here we report expanding this work in three ways: 1. Design of a therapeutic diagnostic PET probe to identify potential suitable cancers for this TRX-based approach. 2. Delivery of targeted anticancer therapeutics in order to gain an additional level of selectivity. 3. Expanding the TRX scaffold to accommodate hydroxamate-containing chemotherapeutics.

TABLE OF CONTENTS

List of Figures and Schemes

Shorthand and abbreviations used in this text

Bpy: bipyridy

CMB: combretastatin

DCM: dichloromethane

DFO: desferrioxamine

DMF: N,N-dimethylformamide

DMS: dimethylsulfide

FAC: ferric ammonium citrate

FAS: ferrous ammonium sulfate

LIP: labile iron pool

PK: pharmacokinetics

PURO: puromycin

ROS: reactive oxygen species

TRX: 1,2,4-trioxolanes

Chapter 1: Mammalian Iron Metabolism

Iron is an essential nutrient for cell growth and proliferation. Cells utilize the redox potential of Fe(II) to perform a variety of cellular processes, including respiration and dNTP production.[1,2] However, free ferrous iron can also undergo Fenton chemistry with water or peroxides found within the cell to generate toxic reactive oxygen species (ROS).[3] Therefore, iron metabolism must be highly regulated in normal, healthy tissues to provide a balance for enough Fe(II) to grow yet not so much as to induce oxidative stress on the cell.

Iron primarily enters the cell through the transferrin receptor complex, in which transferrin bound to two molecules of ferric iron will be bind transferrin receptor and be endocytosed.[4] Upon acidification of the endosome, the Fe(III) is released, reduced by STEAP3, and transported into the cytosol by the divalent metal transporter DMT1. From here, Fe(II) joins the labile iron pool and can behave as a cofactor in nuclear and cytosolic enzymatic processes or transported to the mitochondria where it is incorporated into heme-biosynthesis or packaged into Fe-S clusters.[5] Excess Fe(II) is either oxidized and stored in ferritin or exported through ferroportin.

The concentration of the LIP is regulated through stabilization or repression of mRNA through iron response proteins (IRPs) binding corresponding iron response elements (IREs) in the mRNA.[6,7] IRPs sense if the concentration of free Fe(II) in the cytosol begins to fall outside the acceptable range (approx. 100 nM to 1 uM).[3] In the case of low iron, IRP1 and IRP2 will bind 5' IREs on ferritin and ferroportin, effectively silencing translation, while also binding 3' IREs for transferrin receptor and DMT1 as a

mechanism for mRNA stabilization causing increased translation of these proteins. In the presence of high Fe(II), IRP2 is degraded entirely while IRP1 binds an Fe-S cluster precluding the active site from binding IREs. This allows ferritin and ferroportin mRNA to be translated while transferrin receptor and DMT1 mRNA is destabilized and is degraded.

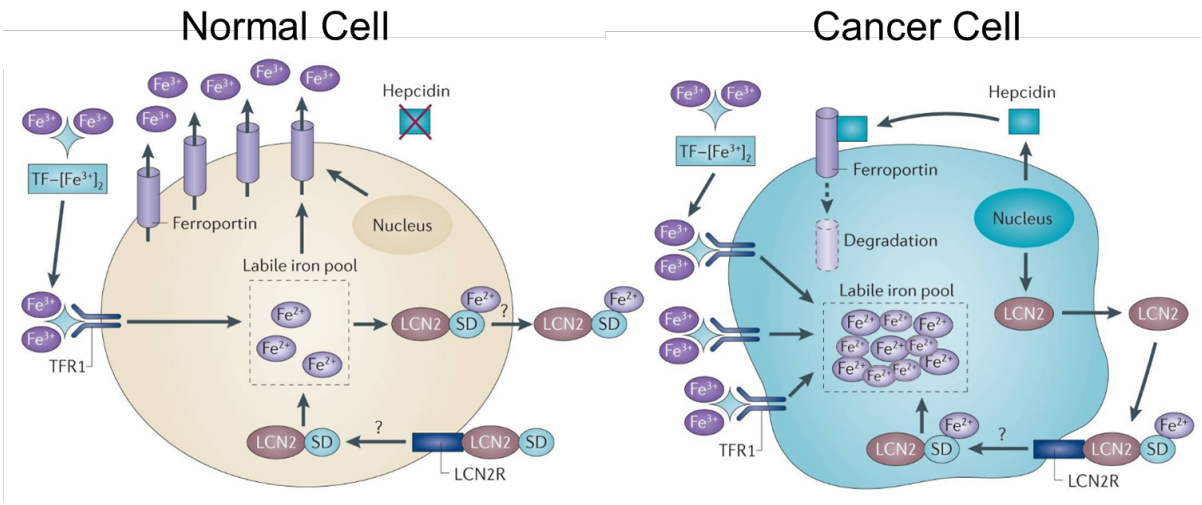

Figure 1-1: Figure adapted from Torti, S. & Torti, F. Nat Rev. Cancer. **2013,** 13, 342-355. Iron metabolism is altered in cancer cells. While healthy cells will keep a tight regulation on the concentration of the labile iron pool (left), many cancers will alter nodes of iron metabolism to hoard excess iron and increase their LIP (right). Examples include an increased transferrin receptor expression and decreased ferroportin expression.

Despite such a tight regulation in healthy cells, many cancers have been known to modulated basal expression of these otherwise highly-regulated protein in this iron metabolism pathway (Figure 1-1). For example, many pancreatic, lung, and prostate cancers are known to upregulate the expression of transferrin receptor while highly aggressive breast cancers have severely decreased expression of ferroportin.[8–11] Most of these aberrant protein expression examples suggest an inverse correlation between a cancer patient's prognosis and the tumor's avidity for iron.[12] While this increased iron

is potentially toxic to the cancer, it also allows the tumor to grow and proliferate more rapidly than otherwise normal tissues.

Within the past few decades, there has been an increased effort in understanding and targeting this aberrant iron metabolism in the cancer patients. Extensive studies were performed in the 1990s attempting to utilize transferrin-drug conjugates to hijack the elevated transferrin receptor levels in cancers, though not with much success.[13,14] More recently clinical trials have been performed dosing cancer patients with iron chelators, or molecules that sequester iron within the cell.[15,16] The Renslo lab has utilized an Fe(II)-activated prodrug platform leveraging the reactivity of the 1,2,4-trioxolane scaffold (TRX) to selectively deliver bulk cytotoxins in preclinical xenograft models, however there is a lack of diagnostic tools to determine Fe(II) levels in a spontaneous tumor.[17,18]

References

1. Torti, S. V & Torti, F. M. Iron and cancer: more ore to be mined. *Nat Rev Cancer* **13**, 342–355 (2013).

2. Wang, J. & Pantopoulos, K. Regulation of cellular iron metabolism. *Biochemical Journal* (2011). doi:10.1042/BJ20101825

3. Kruszewski, M. Labile iron pool: the main determinant of cellular response to oxidative stress. *Mutat. Res. Mol. Mech. Mutagen.* **531**, 81–92 (2003).

4. Abbaspour, N., Hurrell, R. & Kelishadi, R. Review on iron and its importance for human health. *Journal of Research in Medical Sciences* (2014).

5. Philpott, C. C. & Ryu, M.-S. Special delivery: distributing iron in the cytosol of mammalian cells. *Front. Pharmacol.* **5**, 173 (2014).

6. Beinert, H., Kennedy, M. C. & Stout, C. D. Aconitase as iron-sulfur protein, enzyme, and iron-regulatory protein. *Chem. Rev.* (1996). doi:10.1021/cr950040z

7. Muckenthaler, M. U., Galy, B. & Hentze, M. W. Systemic Iron Homeostasis and the Iron-Responsive Element/Iron-Regulatory Protein (IRE/IRP) Regulatory Network. *Annu. Rev. Nutr.* (2008). doi:10.1146/annurev.nutr.28.061807.155521

8. Recalcati, S., Gammella, E. & Cairo, G. Dysregulation of iron metabolism in cancer stem cells. *Free Radic. Biol. Med.* (2018). doi:10.1016/J.FREERADBIOMED.2018.07.015

9. Miller, L. D. *et al.* An iron regulatory gene signature predicts outcome in breast cancer. *Cancer Res.* **71**, 6728–6737 (2011).

10. Marques, O., da Silva, B. M., Porto, G. & Lopes, C. Iron homeostasis in breast cancer. *Cancer Lett.* **347**, 1–14 (2014).

11. Ryschich, E. *et al.* Transferrin receptor is a marker of malignant phenotype in human pancreatic cancer and in neuroendocrine carcinoma of the pancreas. *Eur. J. Cancer* (2004). doi:10.1016/j.ejca.2004.01.036

12. Manz, D. H., Blanchette, N. L., Paul, B. T., Torti, F. M. & Torti, S. V. Iron and cancer: recent insights. *Ann. N. Y. Acad. Sci.* n/a-n/a (2016). doi:10.1111/nyas.13008

13. Li, H. & Qian, Z. M. Transferrin/transferrin receptor-mediated drug delivery. *Medicinal Research Reviews* (2002). doi:10.1002/med.10008

14. Qian, Z. M., Li, H., Sun, H. & Ho, K. Targeted drug delivery via the transferrin receptor-mediated endocytosis pathway. *Pharmacological Reviews* (2002). doi:10.1124/pr.54.4.561

15. Fryknäs, M. *et al.* Iron chelators target both proliferating and quiescent cancer cells. *Sci. Rep.* (2016). doi:10.1038/srep38343

16. List, A. F. Iron overload in myelodysplastic syndromes: diagnosis and

management. *Cancer control : journal of the Moffitt Cancer Center* (2010). doi:10.1177/107327481001701s01

17. Spangler, B. *et al.* A reactivity-based probe of the intracellular labile ferrous iron pool. *Nat. Chem. Biol.* (2016). doi:10.1038/nchembio.2116

18. Spangler, B. *et al.* A Novel Tumor-Activated Prodrug Strategy Targeting Ferrous Iron Is Effective in Multiple Preclinical Cancer Models. *J. Med. Chem.* **59**, 11161–11170 (2016).

Chapter 2: Development of an Fe(II) reactive TRX-based PET imaging agent to detect reactive iron pools *in vivo*

Despite ferrous iron playing such a crucial role in a variety of metabolic activities, and its dysregulation being implied in a multitude of diseases, there remains no method to measure variations in labile Fe(II) *in vivo*. This is due to a variety of factors, such as the difficulty in distinguishing between redox states, a lack of any reliable biomarkers, and the low concentration of ferrous iron.

ABSTRACT

Redox cycling of iron powers various enzyme functions crucial for life, making the study of iron acquisition, storage, and disposition in the whole organism a worthy topic of inquiry. However, despite its important role in biology and disease, imaging iron in animals with oxidation-state specificity remains an outstanding problem in biology and medicine. Here we report a first-generation reactivity-based probe of labile ferrous iron suitable for positron emission tomography studies in live animals. The responses of this reagent to systemic changes in labile iron disposition were revealed using iron supplementation and sequestration treatments in mice, while the potential of this approach for in vivo imaging of cancer was demonstrated using genetically and pathologically diverse mouse models, including spontaneous tumors arising in a genetically engineered model of prostate cancer driven by loss of PTEN.

INTRODUCTION

Iron is a transition metal nutrient whose redox cycling is utilized by iron-dependent enzymes to perform various biological functions essential to life.[1,2] The storage,

transport, and utilization of iron is highly regulated in normal cells and tissues due to the potential of free ferrous iron to promote Fenton chemistry and the formation of reactive oxygen species. Accordingly, iron in biology is stored and transported in an inert ferric state, bound with high affinity by proteins including ferritin (storage) and transferrin (transport). Unloading of iron from transport and storage proteins involves reduction to the soluble ferrous state and entry into the cytosolic labile iron pool (LIP),[3,4] from which iron is utilized to produce essential enzyme cofactors including iron heme[1] and iron−sulfur clusters.[5,6] Dysregulation of iron homeostasis occurs in diverse disease states significantly impacting public health, including neurodegenerative disease,[7] cardiovascular disease,[8] inflammation,[9] and cancer.[10,11] Given its important role in biology and disease, the development of chemical reagents to detect iron with metal ion and oxidation-state specificity is an important problem in chemical biology.[12,13] One of the earliest and most widely used probes, calcein AM, is a chelation-based reagent that unfortunately exhibits poor selectivity for Fe(II) over Fe(III) and other metal ions.[14,15] Improved metal and oxidation-state selectivity was later achieved in the first generation of reactivity-based iron probes, such as Rho-Nox1[16] and IP-1.[17] Subsequently, Renslo and co-workers introduced the reactivity-based probe TRX-PURO,[18] an iron-caged form of puromycin that is activated by Fe(II)-promoted fragmentation of a 1,2,4- trioxolane (TRX) moiety. Immunofluorescence imaging of TRX-PURO treated cells affords improved sensitivity[18] compared to Rho-Nox1 and IP-1, but its use in mice requires the laborious ex vivo analysis of mouse tissues. Caged fluorescent probes are also unsuitable for in vivo studies due to the limited tissue penetration of short wavelength probes.[19,20] Caging of D-aminoluciferin with the TRX moiety used in TRX-PURO

produced the iron probe ICL-1,21 which enables imaging of labile iron in live, luciferase-expressing mice. Despite the advances described above, reactivity-based imaging of labile ferrous iron in nontransgenic animals and humans remains an outstanding problem in biology and medicine. We considered that this challenge might be met in Fe(II)-sensitive, TRX-based radiotracers for positron emission tomography (PET). Incorporation of positron-emitting radionuclides such as fluorine-18 or carbon-11 in biologically active small molecules generally has minimal pharmacological impact.[22] Moreover, PET is used widely in both basic science and clinical settings, affording 3-D noninvasive views of an experimental animal model or human patient.[23] ^{18}F radionuclide is also widely available for routine preclinical and clinical use, and has a convenient 110 min half-life that allows sufficient time for radiotracer preparation and imaging, while ensuring a relatively low radiation dose in patients.[24] The degradation mechanism of 1,2,4-trioxolane antimalarials like artefenomel[25] (Figure 2-1A) has been widely studied, with Fe(II)-promoted cleavage of the peroxide bond and a subsequent β-

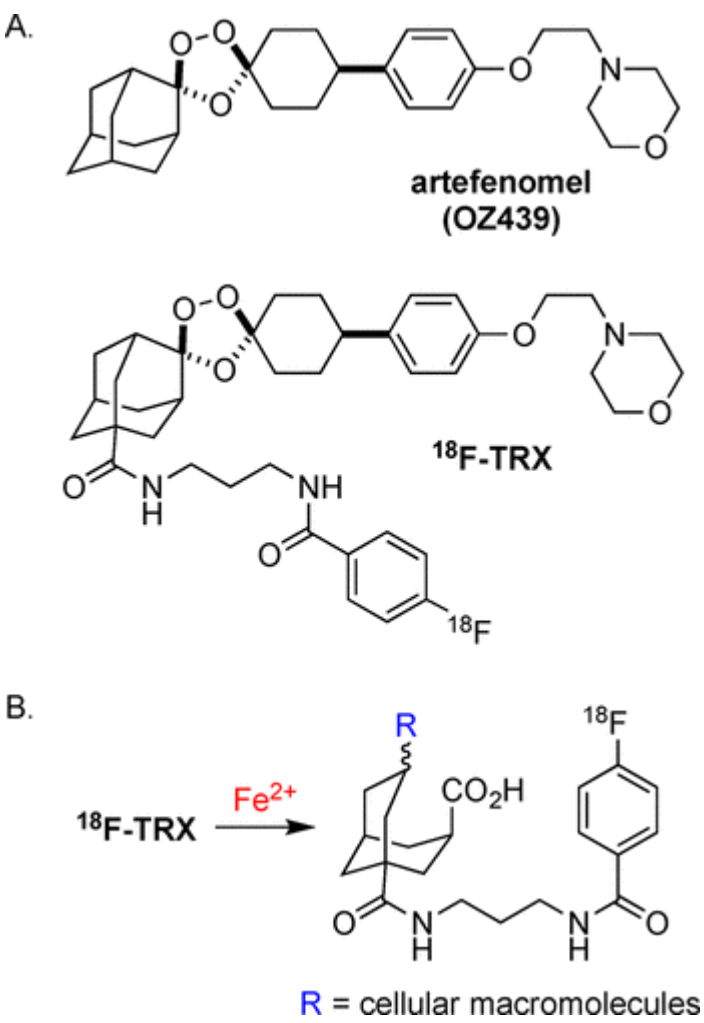

Figure 2-1 (A) Structure of artefenomel and ^{18}F-TRX. (B) Reaction with Fe^{2+} yields ^{18}F-TRX-linked biomolecule adducts that are sequestered in cells at site(s) of reaction.

scission reaction producing carbon-centered radicals that can be intercepted with stable radical reagents like TEMPO,[26] or by nearby biological macromolecules when formed in cells.[27] This radical trapping chemistry thus provides a mechanism by which a putative PET reagent would become sequestered in cells and tissues in an Fe(II)-dependent fashion. Accordingly, we designed the trioxolane-based reagent ^{18}F-TRX in which a short linker bearing ^{18}F is introduced on the adamantane moiety of artefenomel (Figure 2-1A). The 4-fluorobenzamide function in ^{18}F-TRX would be introduced in a final reaction step, using well-established N-succinimidyl-4-[^{18}F]fluorobenzoate radiochemistry. We anticipated that ^{18}F-TRX, like artefenomel, would be stable and well-distributed in vivo, while reacting and becoming sequestered in those cells/ tissues where aberrant concentrations of labile ferrous iron are encountered (Figure 2-1B). Herein, we describe the synthesis of ^{18}F-TRX, a first generation reactivity-based PET probe of labile ferrous iron. We show that this new scaffold retains Fe(II)-dependent reactivity in vitro and accumulates in cells in an Fe(II)- dependent fashion. We describe mouse pharmacokinetic and biodistribution studies in healthy mice with macro- and microdosing, where we observed relatively rapid elimination of ^{18}F-TRX from the blood pool and significant radiotracer uptake in small intestine at 60 min post-injection. The iron sensitivity of ^{18}F-TRX biodistribution *in vivo* was confirmed using iron supplementation and withholding strategies. Finally, we show enhanced accumulation of ^{18}F-TRX in human and mouse tumors (up to ~5% ID/g) compared to normal reference tissue compartments like blood and muscle. Overall, this study marks a first step toward a general method for sensitive and selective imaging of labile iron in living animals and suggests a new approach for functional imaging of cancer.

RESULTS AND DISCUSSION

Radiosynthesis of ^{18}F-TRX

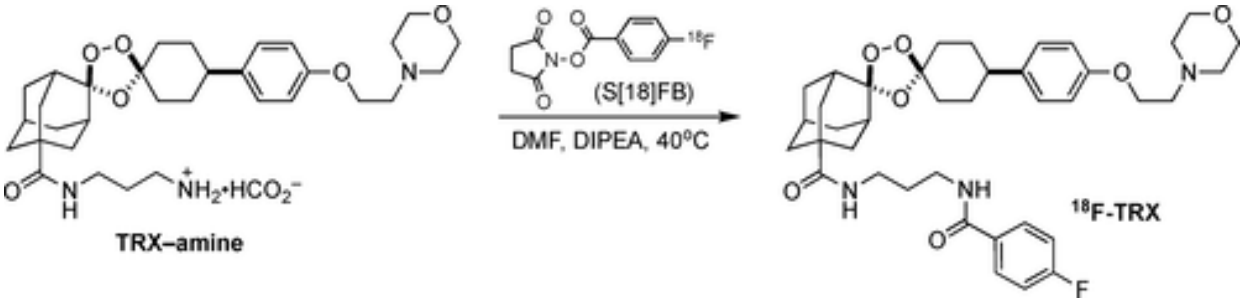

Scheme 2-1: Radiosynthesis of ^{18}F-TRX

The synthesis of ^{18}F-TRX required the novel 1,2,4-trioxolane precursor reagent TRX-amine in which an amine-bearing side chain has been introduced at a bridgehead position on the adamantane ring (Scheme 2-1). This reagent was synthesized in eight steps, based on the general approach described for the synthesis of artefenomel[25] and related antimalarial trioxolanes. The radiosynthesis of ^{18}F-TRX began with the automated preparation of ^{18}F-N-succinimidyl 4-fluorobenzoate. Using an ELIXYS automated radiosynthesizer, ^{18}F-SFB was prepared in 75 min to a decay-corrected radiochemical yield of approximately 70%.[28,29] For the coupling reaction, 20 mCi of ^{18}F-SFB was added to TRX-amine (5 mg of a formate salt) and 10% (v/v) DIPEA in anhydrous DMF (1 mL). The reaction was stirred at 40 °C for 30 min. The reaction produced only one major radioactive peak, which comigrated with the ^{19}FTRX standard (Figure 2-2A). The crude reaction was purified using semipreparative HPLC (1:10

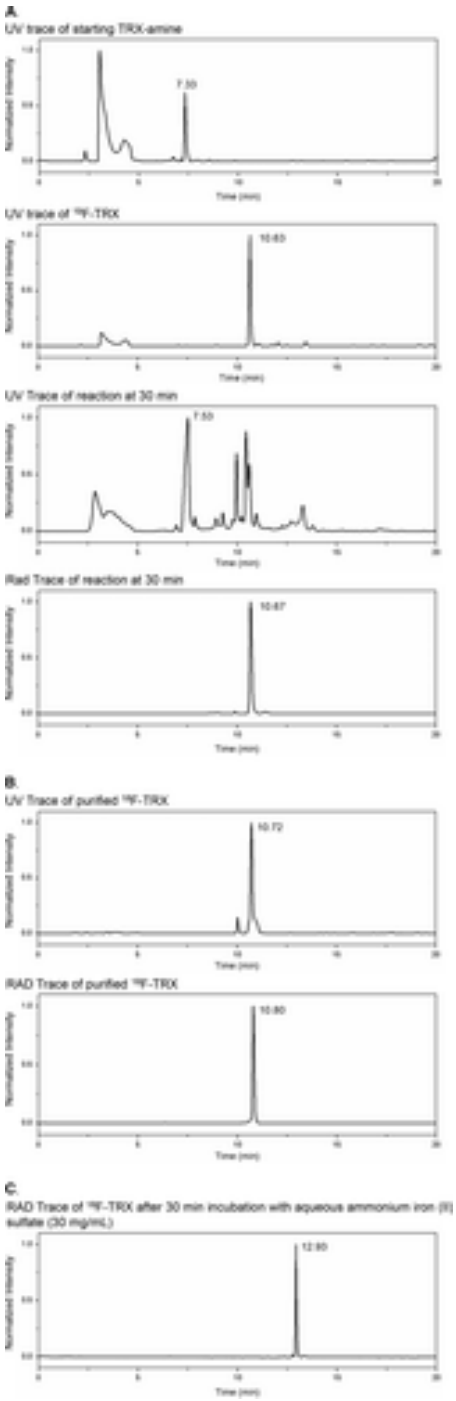

Figure 2-2: Synthesis and isolation of ^{18}F-TRX. (A) Representative semipreparative rad-HPLC traces showing, from top, the UV spectrum at 254 nm for TRX-amine starting material, the UV spectrum at 254 nm for the pure ^{19}F-TRX analytical standard, the UV spectrum at 254 nm for complex radiochemistry reaction mixture at 40 min, and the rad spectrum of the complex radiochemistry reaction mixture at 40 min. Peaks of interest are labeled with the retention time in minutes. (B) Semipreparative rad-HPLC traces of the reinjected fraction isolated after purification. The retention time in minutes of the peak of interest representing ^{18}F-TRX is labeled. (C) A rad spectrum collected 30 min after incubation of ^{18}F-TRX in aqueous ammonium Fe(II) sulfate (30 mg/mL) showing disappearance of the peak corresponding to ^{18}F-TRX and appearance of a new peak with a different retention time.

$CH_3CN:H_2O$ to 19:1 $CH_3CN:H_2O$ over 20 min) to obtain the radiotracer ^{18}F-TRX to a decay-corrected radiochemical yield of 67 ± 7.2%. The purity of the compound was verified by reinjection on semiprep HPLC (Figure 2-2B). 18F-TRX was concentrated, and immediately reconstituted for additional in vitro or animal studies. The specific activity of ^{18}F-TRX was calculated to be 0.052 ± 0.02 Ci/μmol.

In Vitro Studies Show That TRX Analogues React with Fe(II) and Cross-Link Cellular Proteins

To confirm that ^{18}F-TRX retains reactivity with Fe(II), the purified compound was exposed to aqueous ammonium Fe(II) sulfate (FAS, 30 mg/mL). After 30 min, ^{18}F-TRX was entirely consumed and cleanly converted to a single radioactive byproduct as observed on reverse phase rad-HPLC (Figure 2-2C). This result indicates that the reactivity of ^{18}F-TRX with Fe(II) is highly regioselective, as was expected based on earlier mechanistic studies[26] of the antimalarial compounds on which ^{18}F-TRX is based. To confirm that the ^{18}F-bearing side chain in ^{18}F-TRX becomes sequestered in cells following reaction with Fe(II), we prepared the nonradioactive “clickable” probe HC_2-TRX (Figure 2-3A) in which an alkyne function replaces the fluorine atom in ^{18}F-TRX. Fluorescence cell imaging of PC3 cells treated with HC_2-TRX followed by fixing and copper(I)- catalyzed alkyne−azide cycloaddition (CuAAC) reaction with Alexa488-azide were consistent with irreversible labeling of cytoplasmic targets (Figure 2-3B). An in-gel TAMRA fluorescence analysis confirmed the promiscuous labeling of proteins in PC3 cells treated with HC_2-TRX (Figure 2-3C). Moreover, pretreating PC3 cells with ferric ammonium citrate (FAC) or the iron chelator desferrioxamine (DFO) prior to HC_2-TRX revealed more and less labeling, respectively, consistent with iron-dependent activation.

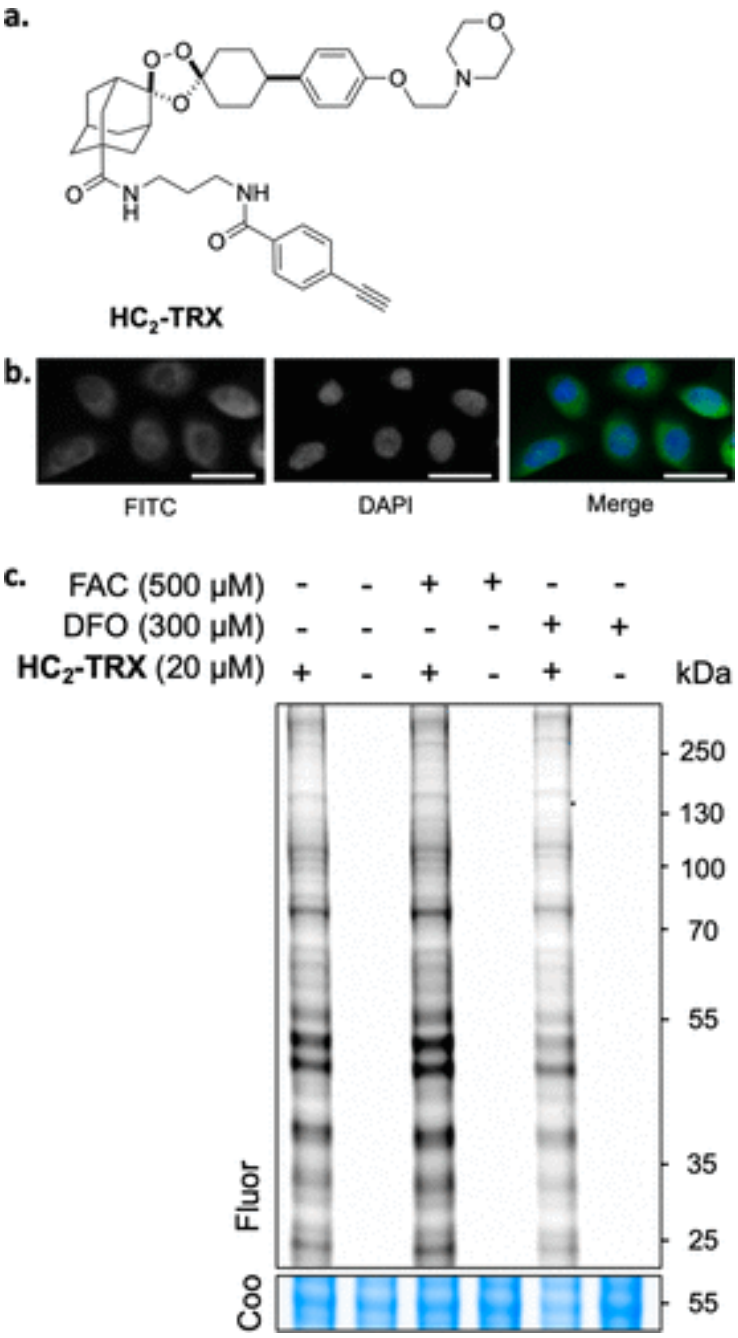

Figure 2-3 Cellular probe HC_2-TRX promiscuously labels proteins in PC3 cells. (A) Structure of cellular "clickable" probe HC_2-TRX. (B) Representative fluorescence images of PC3 cells treated with HC_2-TRX for 6h and visualized by CuACC reaction with Alexa488-azide (green, FITC channel); cell nuclei are visible in the DAPI channel (blue). Scale bars denote 50 μm. (C) In-gel TAMRA fluorescence analysis reveals promiscuous protein labeling following incubation of PC3 cells with HC_2-TRX. Enhanced labeling is observed when PC3 cells were pretreated (2 h) with the Fe(III) source FAC (500 μM) before treatment with HC_2-TRX. Conversely, PC3 cells pretreated with the iron chelator DFO (300 μM) showed reduced labeling intensity. Coomassie (Coo) staining is used as a loading control.

These findings with HC_2-TRX indicate that the analogously positioned ^{18}F atom in ^{18}F-TRX would similarly become sequestered in cells in an Fe(II)-dependent fashion.

^{18}F-TRX Biodistribution Is Fe(II)-Dependent in Normal Mouse Tissues

To determine the biodistribution of ^{18}F-TRX in clinically relevant mouse models, the radiotracer was injected into immunocompetent C57Bl/6J mice and studied over time. Region of interest analysis of a dynamic PET/CT acquisition from 0 to 60 min postinjection revealed several enlightening trends. First, ^{18}F-TRX rapidly cleared from the mediastinal blood pool at a rate ~60 times faster than what we observed from a classic PK assessment of ^{19}F-TRX (Figure 2-4A). Moreover, ^{18}F-TRX rapidly accumulated in liver from 0 to 60 s, suggesting that the radiotracer may be metabolized and cleared through this organ (Figure 2-4B,C) as is the case for artefenomel in humans.[30] Kidney accumulation of the radiotracer was also observed, but the uptake was significantly lower than liver. Moreover, kidney uptake plateaued within 30 s postinjection, suggesting that (as with artefenomel) renal clearance is not the dominant mechanism of clearance of radiotracer. Focal uptake in a region of the small intestine was also observed early after radiotracer injection, and the accumulation steadily increased from 400 to 3600 s. This observation is also consistent with a model of hepatobiliary excretion. To study radiotracer distribution over a broader window of time, ex vivo biodistribution studies were conducted at 30, 60, and 90 min postinjection of ^{18}F-TRX in a separate cohort of mice (Figure 2-4D). These studies generally corroborated the PET findings, showing that ^{18}F-TRX uptake was dominant in the liver, components of the small intestine, and the kidneys. Moreover, radiotracer uptake generally increased from 30 to 90 min in these tissues. Radiotracer uptake was also observed in

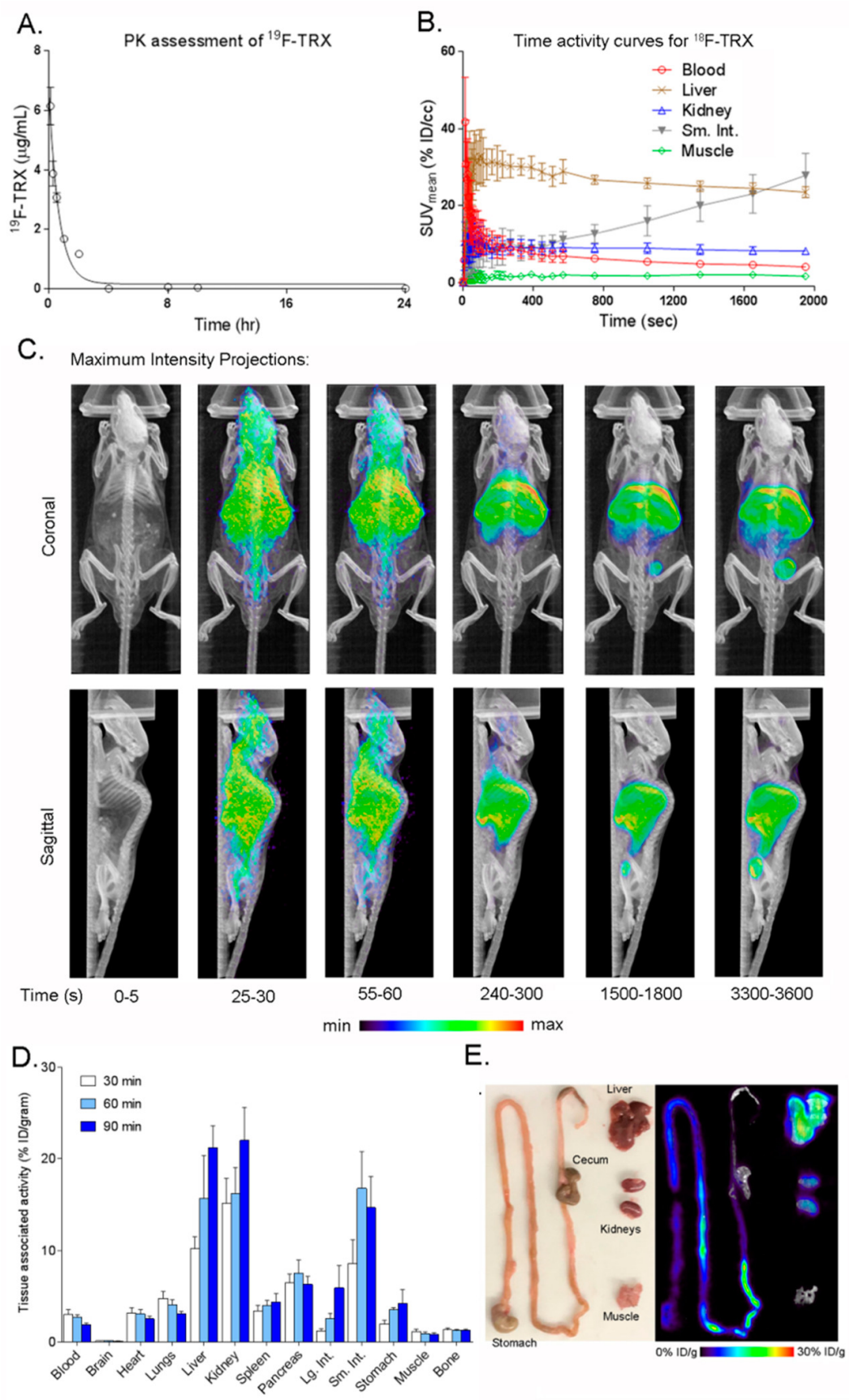
A.
PK assessment of 19F-TRX
19F-TRX (µg/mL)
Time (hr)
B.
Time activity curves for 18F-TRX
Blood
Liver
Kidney
Sm. Int.
Muscle
SUVmean (% ID/cc)
Time (sec)
C.
Maximum Intensity Projections:
Coronal
Sagittal
Time (s)
0-5
25-30
55-60
240-300
1500-1800
3300-3600
min
max
D.
30 min
60 min
90 min
Tissue associated activity (% ID/gram)
Blood
Brain
Heart
Lungs
Liver
Kidney
Spleen
Pancreas
Lg. Int.
Sm. Int.
Stomach
Muscle
Bone
E.
Liver
Cecum
Kidneys
Muscle
Stomach
0% ID/g
30% ID/g

Figure 2-4 An in vivo assessment of the biodistribution of ^{18}F-TRX in tumor naïve immunocompetent mice. (A) Plasma concentration–time curve for ^{19}F-TRX administered via tail vein injection in C57Bl/6J mice revealing a plasma half-life of ∼30 min. (B) Time activity curves derived from region of interest analysis of a 1 h dynamic PET scan reveal radiotracer biodistribution in vivo. The radiotracer rapidly clears from the blood (red) with a calculated serum half-life of about 25 s. The radiotracer is also sequestered within 60 s by the liver (tan) and kidneys (blue), with no additional accumulation from 60 to 3600 s. Liver uptake is significantly higher than what is observed in kidneys. Also, 18F-TRX accumulation in the small intestine (gray) steadily increases from 0 to 3600 s, consistent with a model of hepatobiliary clearance for the radiotracer. Little uptake is observed in the muscle (green). Figure S2C shows the location of the manually drawn regions of interest. (C) Maximum intensity projections sampled serially over short time frames from the dynamic acquisition show the biodistribution of the radiotracer in normal tissues over time. A diffuse signal is observed at early time points, which gradually consolidates into the liver, kidney, and small intestine. (D) Biodistribution data acquired at 30, 60, and 90 min postinjection of ^{18}F-TRX show continuous accumulation of the radiotracer in many abdominal organs. The highest uptake was observed in the liver, kidneys, and small intestine. Radiotracer accumulation was low in the blood pool and muscle, as expected from the MIPs. (E) A PET/CT shows the biodistribution of ^{18}F-TRX in components of the gastrointestinal tract after dissection from a mouse. Prominent uptake was observed in the duodenum and jejunum, while comparatively lower radiotracer uptake was noted in the stomach, ileum, cecum, and large intestine. Liver, kidneys, and muscle are included for perspective on the upper and lower bound of radiotracer uptake in tissues.

the spleen, pancreas, stomach, large intestine, and lungs. Uptake in the brain was very low, consistent with previous observations that other TRX conjugates do not cross the blood−brain barrier.[31] To better understand the localization of the radiotracer within regions of the small intestine, components of the GI tract were excised from a representative mouse 60 min postinjection, and radiotracer biodistribution was assessed with PET/CT (Figure 2-4E). This study suggested that radiotracer uptake was predominant in the duodenum and jejunum. Comparatively lower uptake was observed in the ileum, cecum, and a truncated segment of the large intestine (purged manually to remove fecal matter).

We next tested whether ^{18}F-TRX biodistribution was impacted by exogenous treatments designed to alter tissue concentrations of ferrous iron. 20 minutes prior to i.v. injection of

^{18}F-TRX, immunocompetent mice were treated with an i.p. bolus of PBS, ferric ammonium citrate (FAC, 20 mg/kg), desferrioxamine (50 mg/kg, DFO), deferiprone (50 mg/kg, DFP), or a mixture of FAC (20 mg/kg) precomplexed with desferrioxamine (50 mg/kg, FAC + DFO). The use of a ferric iron source ensures that bioconversion to ferrous iron by normal cellular processes is a necessary prelude to reaction with ^{18}F-TRX. The biodistribution of the radiotracer at 60 min postinjection was strikingly different between treatment arms on PET/CT (Figure 2-5A). For instance, while ^{18}F-TRX most visibly accumulated in the liver of mice treated with PBS, FAC treatment elevated uptake in the liver, small intestine, and gall bladder. Iron depleting strategies (e.g., DFO, FAC + DFO, DFP) reduced radiotracer uptake in the liver, while clearly redistributing ^{18}F-TRX to components of the small intestine. Quantitative biodistribution studies showed a statistically significant increase in ^{18}F-TRX uptake in the liver, spleen, pancreas, and duodenum of mice treated with FAC versus those treated with PBS (Figure 2-5B).

Moreover, treatment with iron chelating agents significantly reduced ^{18}F-TRX uptake in virtually all tissues, with the notable exceptions of the duodenum, ileum, cecum, and large intestine in the FAC + DFO treatment arm. In summary, these data demonstrate that ^{18}F-TRX biodistribution is substantially influenced by exogenous treatments designed to modulate tissue concentrations of ferrous iron. ^{18}F-TRX Detects Tumor Xenografts Sensitive to Trioxolane Prodrugs. We next evaluated if ^{18}F-TRX can detect human tumors derived from cell lines previously shown to harbor sensitivity to TRX-based iron(II)-activatable prodrugs.[32] Biodistribution studies were first conducted in intact male nu/nu mice bearing subcutaneous PC3 xenografts at 30, 60, and 90 min

postinjection of ^{18}F-TRX. The uptake of the radiotracer steadily increased from 30 to 90 min postinjection. Radiotracer levels in the tumor significantly exceeded blood and muscle at 90 min postinjection with a tumor to blood ratio of 1.97 ± 0.4 and a tumor to muscle ratio of 1.90 ± 0.3 (Figure 2-6A). We further tested if ^{18}F-TRX can detect PC3 tumors implanted in the renal capsule, which provides a better vascularized

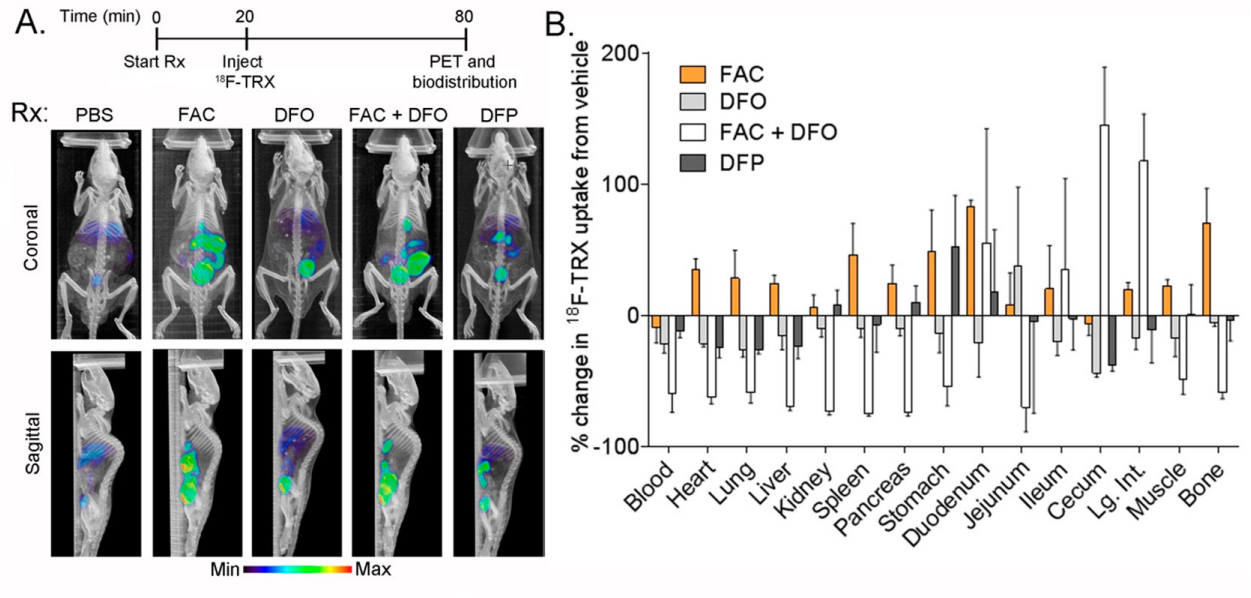

Figure 2-5 ^{18}F-TRX biodistribution is substantially altered by exogenous treatments that change intracellular iron homeostasis. (A) (top) A timeline outlining the sequence of injections in immunocompetent C57Bl/6J mice prior to PET/CT and biodistribution studies. (bottom) Representative maximum intensity projections (MIPs) showing the biodistribution of ^{18}F-TRX in mice from each treatment arm from 50 to 60 min postinjection. Radiotracer uptake was predominantly in the liver of mice pretreated with PBS, while pretreatment with ferric ammonium citrate (FAC) augmented radiotracer uptake in nearly all organs, including the liver and components of the gastrointestinal tract. Pretreatment with various iron depleting agents, including desferrioxamine (DFO), FAC complexed with DFO, and deferiprone (DFP), generally reduced radiotracer uptake in organs and accelerated clearance. The MIPs, while inherently semiquantitative, were derived from decay-corrected PET data with scale bars adjusted to the range 0–50% ID/g to enable gross comparison. (B) Biodistribution data collected at 60 min postinjection show the percent changes in radiotracer uptake for selected organs in each treatment arm compared to mice receiving PBS. Relative increases in radiotracer uptake due to FAC treatment were observed in nearly all organs, while iron depleting treatments generally reduced organ uptake of the radiotracer. Treatment with FAC + DFO enhanced radiotracer uptake in components of the gastrointestinal tract, which may reflect accelerated clearance of the radiotracer.

environment than subcutaneous implants. Biodistribution studies conducted 90 min postinjection of ^{18}F-TRX showed equivalent radiotracer uptake in a PC3 tumor embedded in the renal capsule compared to the extent of uptake in subcutaneous PC3 tumors (Figure 2-6B). ^{18}F-TRX uptake was also significantly higher than background (blood and muscle) in subcutaneous EKVX and U251 tumors, two models of human lung adenocarcinoma and glioblastoma, respectively (Figure 2-6B). The U251 tumor, the model with the highest ^{18}F-TRX uptake, was visually obvious on small animal PET/CT (Figure 2-6C). Ex vivo analysis of the spatial distribution of the radiotracer in U251 tumors showed that ^{18}F-TRX was well-distributed through the tumor xenograft, with the regions of highest uptake appearing to have the densest cellularity on H&E (Figure 2-6D). Collectively, these data show that genetically and pathologically diverse models of human cancer harbor high avidity for ^{18}F-TRX in vivo. We next conducted a pilot imaging study in a genetically engineered mouse model of prostate cancer.[33] A 10 month old Pb-Cre:Ptenfl/fl mouse with invasive adenocarcinoma was treated with ^{18}F-TRX, and after 90 min, the whole prostate was resected post mortem and imaged with PET/CT. Radiotracer uptake was visually higher in the prostate tissue compared to seminal vesicles and muscle (Figure 2-6E). Moreover, ^{18}F-TRX uptake was predominant in the prostate tissue, and not observed in the cysts that routinely develop in this disease model.

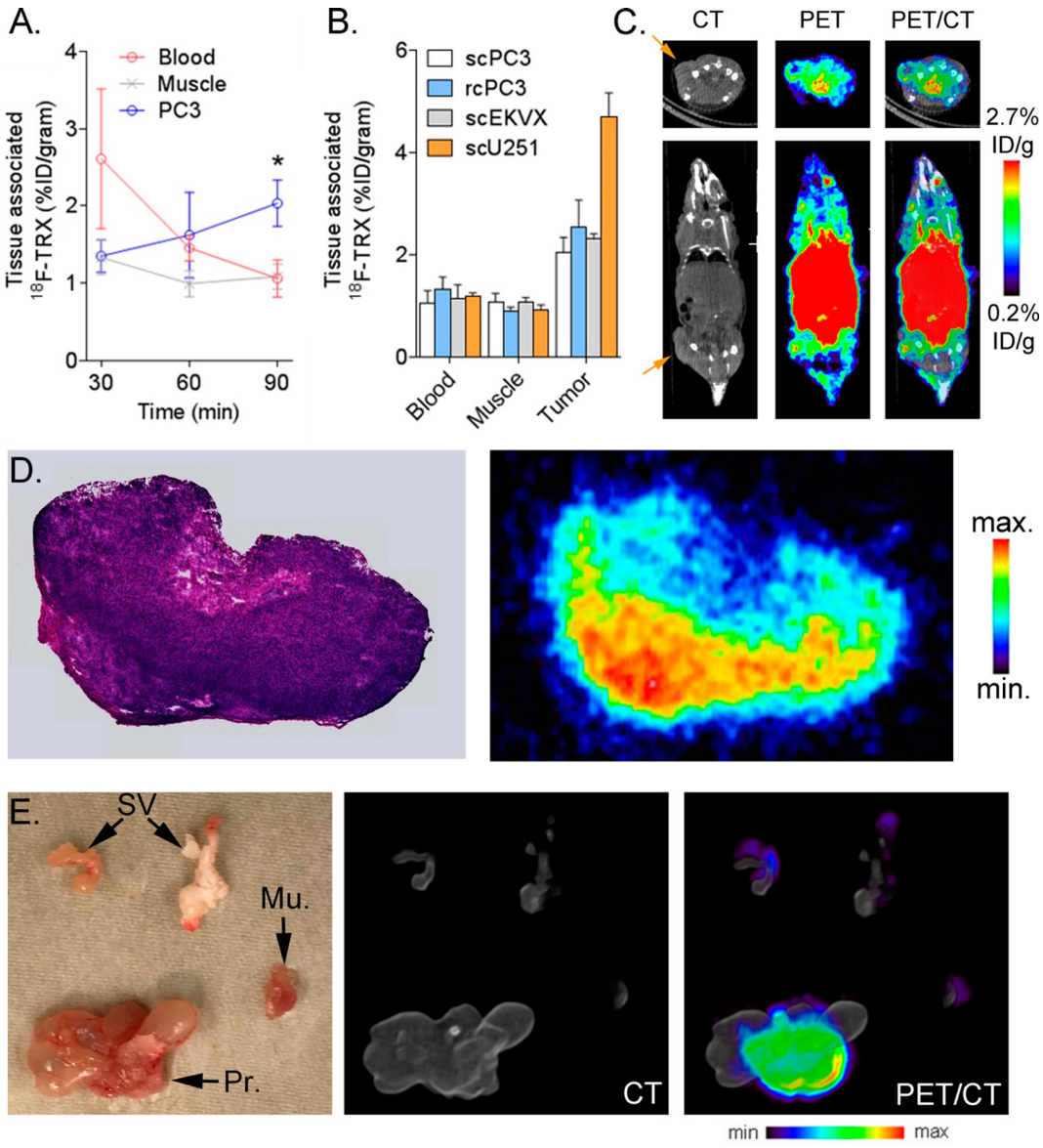

Figure 2-6 ^{18}F-TRX detects tumor tissue in vivo in genetically and pathologically diverse cancer models. (A) Biodistribution data acquired at 30, 60, and 90 min postinjection of ^{18}F-TRX in male nu/nu mice with subcutaneous PC3 xenografts. The radiotracer uptake in the tumor continually increases from 30 to 90 min, consistent with a reactivity-based mechanism of action. Moreover, radiotracer uptake in the tumor exceeds the level observed in blood and muscle at 90 min postinjection, two standard reference compartments for background radiotracer accumulation. The human prostate cancer model PC3 was prioritized as it was previously shown to be highly sensitive to an Fe(II)-sensitive TRX prodrug bearing a chemotherapeutic payload.(32) *P < 0.01 compared to blood and muscle. Figure S4 shows the biodistribution values for the entire repertoire of tissues from this animal cohort as well as the tumor to normal tissue ratios. (B) Biodistribution data acquired 90 min postinjection of ^{18}F-TRX shows radiotracer uptake in tumor exceeding background for PC3 tumors implanted in the renal capsule (rcPC3), and subcutaneous EKVX and U251 tumors (scEKVX, scU251). Figure S5 shows a MR image highlighting the tumor burden in renal capsule. Figure S6 shows the complete biodistribution data sets, and the tumor to normal tissue ratios. (C) PET/CT imaging data showing uptake

of ^{18}F-TRX in tumor and normal tissues for mice bearing subcutaneous U251 tumors. The data were acquired at 90 min postinjection. (D) H&E (left) and digital autoradiography (right) showing ^{18}F-TRX distribution within a representative section of U251 tumors. ^{18}F-TRX appears to be present in all regions of the slice, with the highest relative uptake appearing to colocalize with the area of densest cellularity on H&E. (E) (left) A photograph of the surgically excised whole prostate (Pr.), a piece of muscle from the hindlimb (Mu.), and the seminal vesicles (SV) of a 10 month old Pb-Cre:Pten$^{fl/fl}$ mouse with fully invasive adenocarcinoma. Cysts extending from the anterior prostate are evident by eye. (middle) A volume rendered CT image of the tissues acquired on a small animal PET/CT. (right) A volume rendered PET/CT image of ^{18}F-TRX uptake in the tissues acquired 90 min postinjection of ^{18}F-TRX. The image clearly shows relatively higher accumulation of radiotracer in the diseased prostate compared to muscle or seminal vesicles. ^{18}F-TRX was excluded from the cysts, as expected.

CONCLUSION

Here we reported the design, synthesis, and characterization of ^{18}F-TRX, a reactivity-based PET radiotracer that enables quantitative imaging of labile Fe^{2+} in living animals, including its application to several clinically relevant human and mouse cancer models. Based on an antimalarial with Fe(II)-dependent pharmacology, ^{18}F-TRX can react with Fe^{2+} and become sequestered in tissues at the site(s) of its Fe(II)-promoted activation in vivo. Biodistribution studies and ex vivo imaging revealed high levels of radiotracer uptake in liver and small intestine that could be altered by pretreatment with bioavailable iron sources (FAC) or iron chelators (DFO). Furthermore, ^{18}F-TRX was capable of detecting elevated Fe^{2+} levels in tumor compared to blood pool and muscle in PC3, EKVX, and U251 xenograft models and in a genetic prostate cancer model. These results suggest that labile Fe^{2+} represents an actionable analyte for cancer imaging with PET in animals.

MATERIALS AND METHODS

Radiosynthesis of ^{18}F-TRX

^{18}F-SFB was prepared in 75 min to a decay-corrected radiochemical yield of approximately 70%. ^{18}F-SFB was transferred from the ELIXYS on a C18 SepPak cartridge, and the ^{18}F-SFB was eluted from the cartridge using neat CH_3CN. The acetonitrile was removed under vacuum and a gentle stream of N_2(g), and to the ^{18}F-SFB (20 mCi) was added TRX-amine (5 mg, as formate salt) and 10% (v/v) DIPEA in anhydrous DMF (1 mL). The reaction was stirred at 40 °C. Reaction progress was monitored by radHPLC, and the reaction was terminated at 30 min, as the coupling of ^{19}F-SFB to TRX-amine under analogous conditions was complete at 30 min. The crude reaction was purified using semipreparative HPLC (1:10 CH_3CN:H_2O to 19:1 CH_3CN:H_2O over 20 min) to obtain the radiotracer ^{18}F-TRX to a decay-corrected radiochemical yield of 67 ± 7.2%. The purity of the compound was verified by reinjection on semiprep HPLC.

Cell Culture and Cell/Protein Labeling Experiments

The PC3, EKVC, and U251 cell lines were obtained from ATCC (Manassas, VA) and cultured in Dulbecco's modified Eagle's medium (VWR) supplemented with 10% fetal bovine serum (Gemini Bio) and 1× penicillin/streptomycin (Life Technologies). Cells were cultured at 37 °C supplemented with 5% CO2. For the fluorescence cell imaging experiment, PC3 cells were cultured in a 96-well Greiner μClear plate until reaching 75% confluence. Media was removed and replaced with media containing trioxolane HC_2-TRX (20 μM, 0.1% DMSO) or vehicle (0.1% DMSO). After 6 h, cells were washed

with PBS twice and then fixed with 4% paraformaldehyde for 10 min at room temperature (rt). Cells were washed with PBS twice and incubated with PBS supplemented with 0.1% Triton X-100 for 5 min. Cell were then washed with PBS three times, then incubated for 1 h with click master mix (5 mM sodium ascorbate, 2 mM THPTA, 500 μM CuSO4, 10 μM Alexa488- azide), and then washed with PBS three times. Cells were then treated with PBS containing Hoechst nuclear stain for 10 min, washed with PBS twice, and imaged with an IN Cell 6500 automated cell imager at 40× magnification. For the protein labeling and in-gel fluorescence experiment, PC3 cells were cultured in 6-well plates until reaching 75% confluence. Media was then removed and replaced with fresh media or fresh media containing FAC (500 μM) or DFO (300 μM). After 2 h, media was removed and replaced with media containing HC_2-TRX (20 μM, 0.1% DMSO) or vehicle (0.1% DMSO). After 6 h, cells were washed with PBS twice then incubated in cold PBS for 5 min. Cells were collected using a plastic cell scraper and pelleted. The pellet was resuspended in 100 μL of cold 0.1% NP40 lysis buffer (100 mM Hepes, 150 mM NaCl, 0.1% NP40, pH 7.5) with 5 mg/mL EDTA free protease inhibitor (Roche) for 30 min on ice. The following lysate was centrifuged at 13000 rpm for 10 min. Protein concentration was determined using Pierce BCA protein assay kit (Thermo Fisher) and subsequently normalized to 1 mg/ mL. To 50 μL of this lysate was added the click reaction cocktail (final concentrations: 25 μM TAMRA-Azide, 1 mM $CuSO_4$, 0.1 mM TBTA, 1 mM TCEP), and it was incubated at room temperature for 1 h in the dark. Protein was precipitated by addition of 1 mL of cold methanol and cooled to −80 °C. Protein was pelleted by centrifugation at 14000 rpm for 5 min at 4 °C. Methanol was decanted, and the protein pellet was washed with 1 mL of cold methanol and

pelleted again as described. Methanol was decanted, and the pellet was resuspended in 50 µL of 1× laemmli buffer (Bio-Rad) supplemented with β-mercaptoethanol. Sample was boiled for 5 min, and 25 µg of protein was loaded onto Bolt 4−12% Bis-Tris Plus Gel (Thermo Fisher). Fluorescence was visualized by a ChemiDoc system and displayed in a grayscale. Following imaging, total protein was visualized by Coomassie stain.

Animal Experiments

To reconstitute ^{18}F-TRX for animal studies, the probe was trapped on a C18 Sep-Pak cartridge, and eluted with a small volume of ethanol. Ethanol was removed at 50 °C under vacuum and a gentle stream of N_2 (g) to afford neat ^{18}F-TRX. Formulation of ^{18}F-TRX for in vivo studies proved challenging due to the very poor aqueous solubility of this material. After some experimentation, we adopted a formulation comprising 10% DMSO in a 20 mM aqueous sodium phosphate solution at pH 3 used previously by Charman and co-workers[25] for IV pharmacokinetic studies of artefenomel. A 5 mg/kg dose of ^{19}F-TRX in 100 µL of this formulation was well-tolerated in mice when administered by tail vein injection. All animal experiments were conducted under the approval from Institutional Animal Care and Use Committee (IACUC) at UCSF. Male nu/nu or C57BL6/J mice (4−6 weeks) were purchased from Charles River. All the mice were well-housed in the USCF with free access to food and water. Nu/nu mice were inoculated with 2−5 x 10^6 PC3 cells in a mixture of media (RPMI) and Matrigel (Corning) (1:1 v/v) subcutaneously into one flank. Tumors in mice were palpable within 3−4 weeks after the implanting. Male Rag2 RAGN12 mice (Taconic) were used for the renal capsule tumor implants. The mice were anesthetized with isofluorane (2−3%) and

performed with a dorsal midline incision (0.5 cm). Via pressuring on the muscle wall, one kidney was pulled gently and carefully through the small incision. PC3 tumor cells (5 × 106 in 50 mL of PBS) were then injected into the pocket under the kidney capsule, which was lifted from the kidney parenchyma. The kidney was placed back to the body of mice, and then the skin incision was closed using 3 surgical sutures. Carprofen (5−10 mg/kg) was used to treat the mice for easing recovery. Mice were observed carefully over 24 h for the signs of postoperative bleeding, pain, and (or) other complications. After surgery, a 14 T Agilent small animal MRI was used to monitor the tumor progression for the following 7−14 days. Small Animal PET/CT. ^{18}F-TRX (∼300 μCi) was injected via tail vein in 100−150 μL of 10% DMSO in a 20 mM aqueous sodium phosphate solution. For treatment studies, vehicle (100 μL PBS), FAC (20 mg/kg in PBS, 100 μL), both FAC (20 mg/kg in PBS, 100 μL) and DFO (50 mg/kg in PBS, 100 μL), DFP (30 mg/kg in PBS, 100 μL), or DFO (30 mg/kg in PBS, 100 μL) were injected intraperitoneally 20 min prior to the intravenous injection of 18F-TRX. The mice were anesthetized with 2−3% isoflurane, and imaged with a Siemens Inveon microPET/CT. For dynamic acquisitions, the mice were anesthetized prior to injection, and injected while positioned on the scanner bed. All imaging data were decay-corrected, reconstructed, and analyzed with AMIDE software. Maximum intensity projections (MIPs) were generated by AMIDE software. Regions of interest (ROI) were manually placed to calculate SUV data from the dynamic acquisitions. Biodistribution Studies. Mice were euthanized with CO_2 (g) asphyxiation and dissected at dedicated time points postinjection. The blood and tissues were removed, washed, dried, and weighed. The activity of each tissue was measured with a γ counter. All data were decay-corrected.

PRISM software was used to express a percentage (% ID/g) of the injected dose per gram of tissue. Digital Autoradiography. Postmortem, tumors were flash frozen in OCT on liquid nitrogen. The tissue was sectioned with a microtome into 20 μm thickness slices and mounted on glass slides. The slides were exposed in a GE phosphor storage screen for 10 radionuclide half-lives. The phosphor screen was developed on an Amersham Typhoon 9400 phosphorimager. The images were processed using ImageJ software. H&E staining was performed by the Pathology core facility at UCSF. Statistics. All statistical analysis was performed using PRISM v6.0 or ORIGIN software. An unpaired, two-tailed Student's t test was used to determine statistically significant differences in the data. Changes at the 95% confidence level ($P < 0.05$) were reported as statistically significant.

SUPPORTING INFORMATION

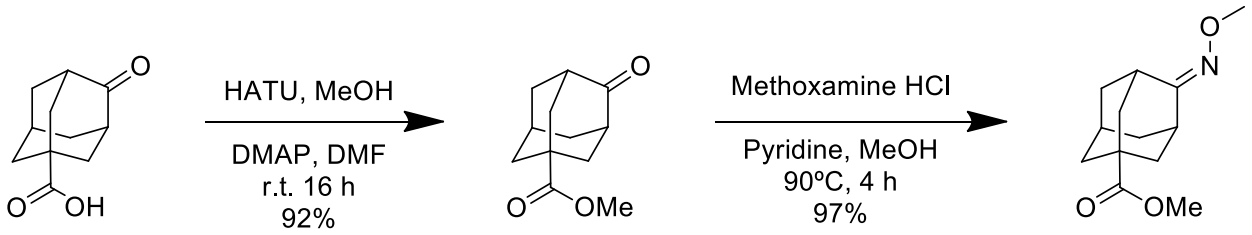

Scheme S2-1: Synthesis of adamantane oxime **2**

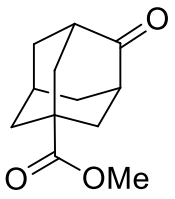

Synthesis of methyl 4-oxoadamantane-1-carboxylate (1). To a round bottom flask containing a Teflon-coated magnetic stir bar under an Ar(g) atmosphere was added 4-oxoadamantane-1carboxylic acid (3.885 g, 20.0 mmol, 1.0 equiv.), HATU (9.219 g, 24.0 mmol, 1.2 equiv.), N,Ndimethylformamide (80 mL), methanol (8.103 ml, 200.0 mmol, 10.0 equiv.), and 4dimethylaminopyridine (1.222 g, 10.0 mmol, 0.5 equiv.). After addition of the HATU, the solution turned a dark orange color. The solution was allowed to at room temperature for 16 hours. Based on TLC and LCMS analysis, the reaction was complete. To this reaction was added DI Water (75 mL). The aqueous layer was then extracted with ethyl acetate (3 x 75 mL). The organic layers were collected and washed with brine (3 x 75 mL) to remove excess DMF. The organic layer was dried over magnesium sulfate and filtered under vacuum. Organic solvent was removed under reduced pressure to give a dark brown solution in residual DMF. This crude product was purified through flash column chromatography (330 g HP silica gel cartridge, 0– 20% EtOAc/Hexanes, product eluted during 20% EtOAc/Hex) to yield methyl 4-oxoadamantane-1-carboxylate (**1**, 3.869 g, 93%) as a white, crunchy solid. ^{1}H NMR signals were consistent with reported values.[34]

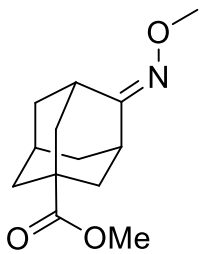

Synthesis of methyl-4-(methoxyimino)adamantane-1-carboxylate (2). To a sealed tube containing a Teflon-coated magnetic stir bar under an Ar(g) atmosphere was added methyl 4oxoadamantane-1-carboxylate (**1**, 3.800 g, 18.2 mmol, 1.0 equiv.) and methanol (36 mL). This solution was stirred until all solid had dissolved, then pyridine (2.946 ml, 36.5 mmol, 2.0 equiv.) and methoxylamine HCl (1.711 g, 20.1 mmol, 1.1 equiv.) were added sequentially. The solution was again stirred at room temperature under argon until all of the solid went into solution. The reaction was played in an oil bath that had been preheated to 90°C and stirred for 4 hours. The solution was allowed to cool at which point TLC and LCMS analysis showed the reaction to be complete. The mixture was concentrated under reduced to give a white slurry. Following the addition of EtOAc (50 mL) and DI water (50 mL), the organic layer was collected and washed with $KHSO_4$ (2 x 50 mL) and brine (1 x 50 mL). The organic layer was dried over $MgSO_4$ and filtered. The mixture was concentrated under reduced to afford methyl-4(methoxyimino)adamantane-1-carboxylate (**2**) as a white fluffy powder (4.186g, 97%). ^{1}H NMR signals were consistent with reported values.[34]

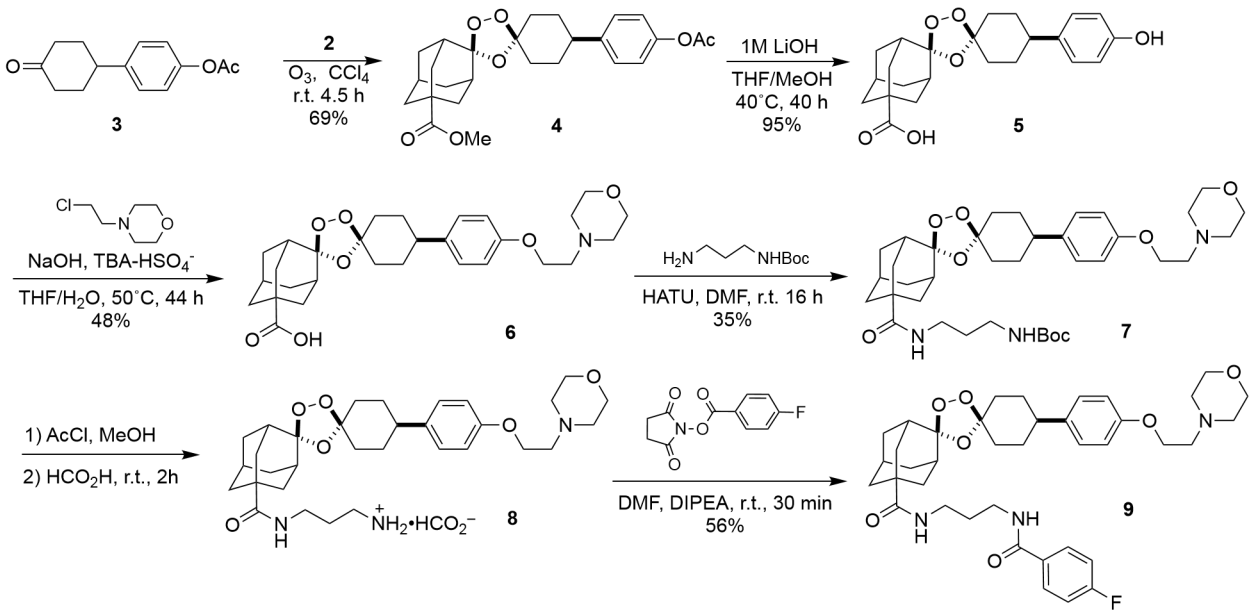

Scheme S2-2. Synthesis of TRX-amine and ^{19}F-TRX

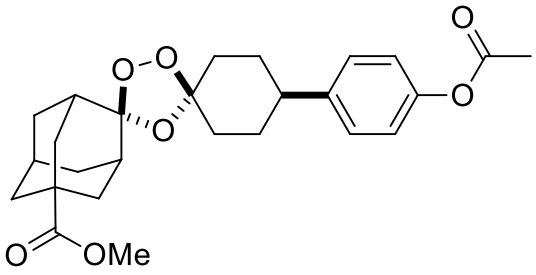

Synthesis of methyl-4''-(4-acetoxyphenyl)dispiro[adamantane-2,3'-[1,2,4]trioxolane-5',1''cyclohexane]-5-carboxylate (4). To a round bottom flask containing a Teflon-coated magnetic stir bar open to the atmosphere was added methyl-4-(methoxyimino)adamantane-1-carboxylate (**2**,1.277 g, 5.4 mmol, 1.0 equiv.) and 4-(4-acetoxyphenyl)cyclohexan-1-one (**3,** 1.250 g, 5.4 mmol, 1.0 equiv.). To the mixture of solid materials was added carbon tetrachloride (100 mL) and dichloromethane (5 mL). This solution was cooled to 0˚C and subsequently sparged with O_2 for 10 minutes. The

reaction was kept at 0 ˚C while ozone was then bubbled (2 L/min, 35% power). Over the following 3 hours, an additional 0.5 equivalents of oxime was added until the reaction was determined to be complete. The reaction was purged with O_2 for 10 minutes in an effort to remove any dissolved ozone, followed by sparging with argon gas for 10 minutes to remove any dissolved oxygen. The reaction mixture was concentrated under reduced pressure to give a white slurry. This crude mixture was purified through flash column chromatography (0– 10% EtOAc/Hexanes) to yield methyl-4''-(4-acetoxyphenyl)dispiro[adamantane-2,3'[1,2,4]trioxolane-5',1''-cyclohexane]-5-carboxylate (**4**, 1.68 g, 69%) as an off-white foam. Analysis by LCMS and NMR indicates a mixture of diasteromers (ca. 8:1). ^{1}H NMR (400 MHz, CDCl3) δ 7.25 (d, 8 Hz, 2H, minor diastereomer), 7.21 (d, 8 Hz, 2H, major), 7.05-6.97 (m, 2H), 3.70-3.65 (m, 3H), 2.62-2.51 (m, 1H), 2.29 (s, 3H), 2.26–2.19 (m, 2H), 2.17–1.79 (m, 16H), 1.77–1.64 (m, 4H); ^{13}C NMR (100 MHz, CDCl3) δ 177.1, 176.1 (minor diastereomer), 169.5, 148.8, 143.4, 127.6, 121.3, 110.1, 108.5, 51.9, 51.6 (minor diastereomer), 42.2, 40.2, 40.0, 39.8, 39.4, 38.2, 38.0 (minor diastereomer), 37.7, 36.2, 36.1 (minor diastereomer), 35.9, 35.8 (minor diastereomer), 34.5, 33.6, 31.3, 27.2, 26.5, 26.1, 24.6, 21.0.; MS (ESI) calculated for $C_{26}H_{32}O_7$ $[M + Na]^+$ m/z 479.20, found 479.08.

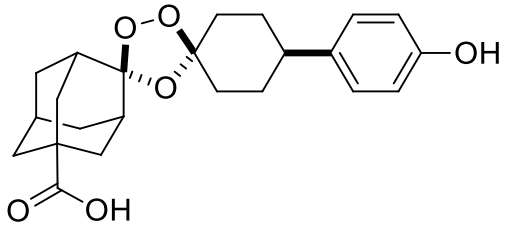

Synthesis of 4''-(4-hydroxyphenyl)dispiro[adamantane-2,3'-[1,2,4]trioxolane-5',1''cyclohexane]-5-carboxylic acid (5). To a round bottom flask containing a Teflon-coated magnetic stir bar open to the atmosphere was added methyl-4''-(4-acetoxyphenyl)dispiro[adamantane-2,3'-[1,2,4]trioxolane-5',1''-cyclohexane]-5-carboxylate (**4**, 1.685 g, 3.7 mmol, 1.0 equiv.) dissolved in anhydrous tetrahydrofuran (40 mL) and methanol (40 mL). To this stirring solution was 1M lithium hydroxide in water (14.8 ml, 14.8 mmol, 4.0 equiv.). The reaction was placed into an oil bath that had been preheated to 40˚C and was allowed to stir for 40 hours under argon at which point the reaction was determined to be complete. The reaction was concentrated under reduced pressure to give a white slurry. DI water (75 mL) and EtOAc (75 mL) were added to the crude mixture and transferred to an Erlenmeyer flask containing a Teflon-coated magnetic stir bar and cooled to 0˚C. The pH of this stirring mixture was adjusted to 1 by dropwise addition of 1N HCl. The organic layer was collected and the aqueous layer was extracted with EtOAc (2 x 75 mL). The organic layers were combined and washed with brine (1 x 50mL). The organic layer was concentrated under reduced pressure to yield 4''-(4-hydroxyphenyl)dispiro[adamantane-2,3'-[1,2,4]trioxolane-5',1''-cyclohexane]-5-carboxylic acid (**5**, 1.4g, 95%) as a white powder. ^{1}H NMR (400 MHz, DMSO-d6) δ 12.18 (br s, 1H), 7.21 (br s, 1H), 7.05-6.96 (m, 2H), 6.71-6.64 (m, 2H), 2.50-2.40 (m, 1H), 2.14–1.97 (m, 5H), 2.17–1.79 (m, 14H), 1.58–1.43 (m, 2H); ^{13}C NMR (100 MHz, DMSO-d6) δ 177.6, 176.9 (minor diastereomer), 155.5, 136.1 127.4 (minor diastereomer), 127.3 115.0, 109.7, 108.4, 45.3, 40.7, 39.7, 38.8, 38.4, 37.7, 37.6 (minor diastereomer), 37.5, 37.3, 36.0, 35.9 (minor diastereomer), 35.5, 35.4 (minor

diastereomer), 34.1, 33.2, 31.4, 26.8, 26.0, 25.6; MS (ESI) calculated for $C_{23}H_{28}O_6$ [M - H]$^-$ m/z 399.18, found 399.23.

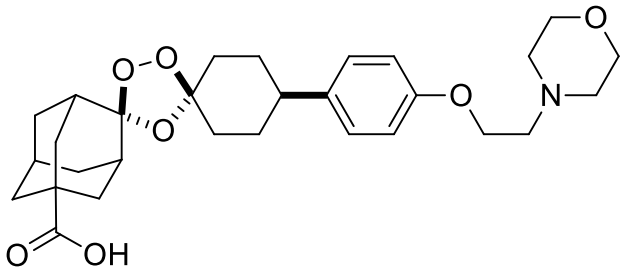

Synthesis of 4''-(4-(2-morpholinoethoxy)phenyl)dispiro[adamantane-2,3'-[1,2,4]trioxolane5',1''-cyclohexane]-5-carboxylic acid (6). To a round bottom flask containing a Teflon-coated magnetic stir bar under Ar(g) was added 4''-(4-hydroxyphenyl) dispiro[adamantane-2,3'[1,2,4]trioxolane-5',1''-cyclohexane]-5-carboxylic acid (**5**, 1.400 g, 3.5 mmol, 1.0 equiv.), 1M sodium hydroxide (31.5 ml, 31.5 mmol, 9.0 equiv.) and tetrabutylammonium bisulfate (0.237 g, 0.7 mmol, 0.2 equiv.). This mixture was allowed to stir for 30 minutes at room temperature under argon, at which point 4-(2-chloroethyl)morpholine hydrochloride (1.301 g, 7.0 mmol, 2.0 equiv.) was added. The reaction was placed into an oil bath that had been preheated to 50˚C. Over the following 36 hours, an additional 3 equivalents of morpholine and sodium hydroxide were added starting material was no longer observed by LCMS. 1M NaOH (21 mL, 21 mmol, 6 eq) was then added in one portion and the reaction was allowed to stir at 50˚C for 4 hrs. At this point the reaction was determined to be complete by LCMS and the solution was concentrated under reduced vacuum to give a white slurry. To this crude mixture was added deionized water (75 mL) and EtOAc (75 mL). Following the addition of EtOAc, it was noted that a white precipitate had formed. This solid was filtered to give the product 4''-(4-(2morpholinoethoxy)phenyl)dispiro[adamantane-2,3'-[1,2,4]trioxolane-5',1''-

cyclohexane]-5carboxylic acid (**6**, 880 mg, 1.71 mmol, 49%) as a white powder. ^{1}H NMR (400 MHz, CDCl3) δ 8.60 (br s, 1H), 7.18-7.09 (m, 2H), 6.88-6.80 (m, 2H), 4.16-4.08 (m, 2H), 3.80-3.71 (m, 4H), 2.85 (t, 5.2 Hz, 2H), 2.72-2.63 (m, 4H), 2.54-2.45 (m, 1H), 2.27-2.17 (m, 2H), 2.14–1.78 (m, 15H), 1.77–1.63 (m, 4H); ^{13}C NMR (100 MHz, $CDCl_3$) δ 181.3, 181.0 (minor diastereomer), 156.9, 138.6, 127.7, 114.5, 110.3, 108.7, 66.4, 66.3 (minor diastereomer), 65.1, 65.0 (minor diastereomer), 57.4, 53.7, 53.6 (minor diastereomer), 42.1, 42.0, 41.4, 39.7, 39.2, 38.1, 38.0, 36.3, 36.1, 35.9, 34.7, 34.6 (minor diastereomer), 34.2, 33.7, 31.7 (minor diastereomer), 31.6, 26.6, 26.2; MS (ESI) calculated for $C_{29}H_{39}NO_7$ $[M + H]^+$ m/z 514.28, found 514.18.

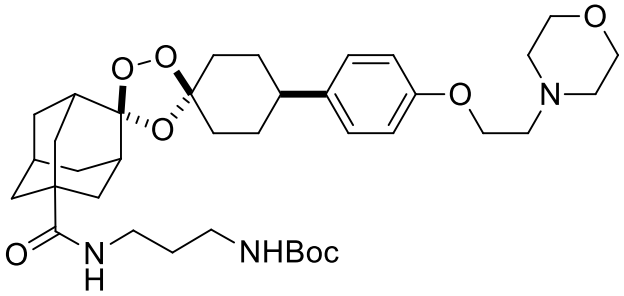

Synthesis of (tert-butyl N-{3-[(4''-{4-[2-(morpholin-4-yl)ethoxy]phenyl} dispiro[adamantane-2,2'-[1,2,4]trioxolane-4',1''-cyclohexane]-7-yl)formamido]propyl} carbamate (7). To a round bottom flask containing a Teflon-coated magnetic stir bar under Ar(g) was added 4''-(4-(2-morpholinoethoxy)phenyl)dispiro[adamantane-2,3'-[1,2,4]trioxolane-5',1''cyclohexane]-5-carboxylic acid (**6**, 800 mg, 1.6 mmol, 1.0 equiv.), HATU (710 mg, 1.9 mmol, 1.2 equiv.), N,N-diisopropylethylamine (0.678 ml, 3.9 mmol, 2.5 equiv.) and N,N-dimethylformamide (15 mL). This dark orange solution stirred at room temperature under argon for 5 minutes before N-Boc-1,3-propanediamine (326 mg, 1.9 mmol, 1.2

equiv.) was added in one portion. The reaction was allowed to stir at room temperature for 16 hours at which point LCMS confirmed that the reaction had reached completion. The crude reaction was purified by preparatory HPLC (Waters XBridge C18 column, 25-70% methanol/water with 0.05% formic acid) to afford (tert-butyl N-{3-[(4''-{4-[2-(morpholin-4-yl)ethoxy]phenyl}dispiro[adamantane2,2'-[1,2,4]trioxolane-4',1''-cyclohexane]-7-yl)formamido]propyl}carbamate (**7**, 365mg, 0.55mmol, 35%) as a white powder. This purification allowed separation of the roughly equal mixture of diastereomers, of which only the high Rf isomer was characterized and taken forward. ^{1}H NMR (400 MHz, CDCl3) δ 7.14-7.09 (m, 2H), 6.86-6.82 (m, 2H), 4.09 (t, 5.8 Hz, 2H), 3.74 (t, 4.6 Hz, 4H), 3.30 (q, 6.3 Hz, 2H), 3.19-3.12 (m, 2H), 2.80 (t, 5.8 Hz, 2H), 2.61-2.55 (m, 4H), 2.55-2.45 (m, 1H), 2.23-2.16 (m, 2H), 2.14–2.09 (m, 2H), 2.07-1.77 (m, 15H), 1.77–1.56 (m, 6H), 1.46 (s, 9H); ^{13}C NMR (100 MHz, CDCl3) δ 177.3, 157.1, 156.7, 138.5, 127.6, 114.5, 110.3, 108.9, 66.9, 65.7, 57.7, 54.0, 42.0, 39.8, 38.5, 38.0, 36.9, 36.7, 36.2, 34.7, 33.7, 31.6, 28.4, 26.4; MS (ESI) calculated for $C_{37}H_{55}N_3O_8$ [M + H]$^{+}$ m/z 670.41, found 670.35.

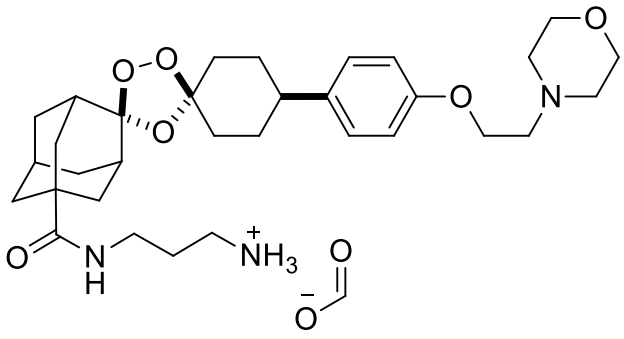

Synthesis of N-(3-ammoniumpropyl)-4''-{4-[2-(morpholin-4-yl)ethoxy]phenyl}dispiro[adamantane-2,2'-[1,2,4]trioxolane-4',1''-cyclohexane]-7-

carboxamide formate (8, TRX-amine). To a round bottom flask containing a Teflon-coated magnetic stir bar under Ar(g) was added (tert-butyl N-{3-[(4''-{4-[2-(morpholin-4-yl)ethoxy]phenyl}dispiro[adamantane-2,2'[1,2,4]trioxolane-4',1''-cyclohexane]-7-yl)formamido]propyl}carbamate (**7,** 225 mg, 0.3 mmol, 1.0 equiv.) and methanol (7.5 mL). To this stirring solution was added acetyl chloride (0.72 ml, 10.1 mmol, 30.0 equiv.) dropwise over 5 minutes. The reaction was allowed to stir at room temperature for 140 minutes at which point the reaction was determined to be complete by LCMS. To quench the reaction, the pH was adjusted to pH 7 through addition of saturated $NaHCO_3$ (10 mL). The mixture was concentrated under reduced pressure to give a white slurry. To this slurry was added 1M Na_2CO_3 (20 mL) and CH_2Cl_2 (40 mL). The organic layer was collected and the aqueous layer was extracted with CH_2Cl_2 (2 x 25 mL). The combined organic layers were transferred to an Erlenmeyer flask equipped with a stir bar to which was added water (75 mL). This stirring mixture was cooled to 0˚C and the pH was adjusted to 1 through addition of formic acid. The aqueous layer was collected and washed with CH_2Cl_2 (2 x 40mL). N-(3ammoniumpropyl)-4''-{4-[2-(morpholin-4-yl)ethoxy]phenyl}dispiro[adamantane-2,2'-[1,2,4]trioxolane-4',1''-cyclohexane]-7-carboxamide formate (**8**, 218 mg, 100%) was obtained as a white fluffy solid following lyophilization of the aqueous layer. Characterization was of a mixture of isomers. ^{1}H NMR (400 MHz, $CDCl_3$) δ 7.13-7.04 (m, 2H), 6.86-6.77 (m, 2H), 4.07-4.02 (m, 2H), 3.71-3.66 (m, 4H), 3.37-3.28 (m, 2H), 2.77-2.72 (m, 2H), 2.56-2.51 (m, 4H), 2.502.40 (m, 1H), 2.16-2.09 (m, 2H), 2.07-1.74 (m, 19H), 1.72–1.55 (m, 4H); ^{13}C NMR (100 MHz, CDCl3) δ 177.2, 157.0, 138.3, 127.5, 114.3, 110.2, 108.6, 66.8, 65.7, 57.6,

54.0, 41.8, 39.6, 39.2, 38.4, 37.8, 36.6, 36.1, 36.0, 34.5, 33.6, 31.5, 26.3; MS (ESI) calculated for $C_{32}H_{47}N_3O_8$ $[M + H]^+$ m/z 570.35, found 570.21.

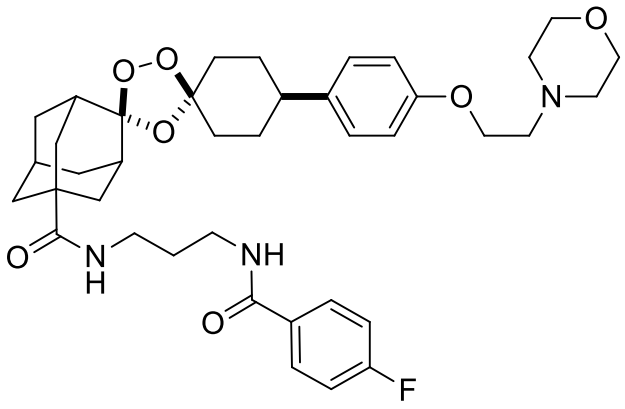

Synthesis of N-(3-(4-fluorobenzamido)propyl)-4''-(4-(2-morpholinoethoxy)phenyl) dispiro[adamantane-2,3'-[1,2,4]trioxolane-5',1''-cyclohexane]-5-carboxamide (9, ^{19}F-TRX analytical standard). To a round bottom flask containing a Teflon-coated magnetic stir bar under Ar(g) was added N-(3-ammoniumpropyl)-4''-{4-[2-(morpholin-4yl)ethoxy]phenyl} dispiro[adamantane-2,2'-[1,2,4]trioxolane-4',1''-cyclohexane]-7-carboxamide formate (**8**, 10 mg, 0.018 mmol, 1.0 equiv.), N,N-diisopropylethylamine (0.006 ml, 0.033 mmol, 1.9 equiv.) and N,N-dimethylformamide (0.2 mL). To this stirring solution was added SFB (4 mg, 0.018 mmol, 1.0 equiv.) in one portion. The reaction was lowered into an oil bath that had been preheated to 50˚C and was allowed to stir under argon for 30 minutes. At this point, the reaction was determined to be complete by LCMS. The crude reaction was purified by preparatory HPLC (Waters XBridge C18 column, 40-70% methanol/water with 0.05% formic acid) to afford N-(3-(4-fluorobenzamido)propyl)-4''-(4-(2morpholinoethoxy)phenyl)dispiro[adamantane-2,3'-[1,2,4]trioxolane-5',1''-cyclohexane]-5carboxamide **(9, ^{19}F-TRX)** as a white powder (7

mg, 58%). ^{1}H NMR (400 MHz, CDCl3) δ 7.957.88 (m, 2H), 7.17-7.09 (m, 4H), 6.87-6.82 (m, 2H), 4.14-4.07 (m, 2H), 3.78-3.71 (m, 4H), 3.48-3.34 (m, 4H), 3.19-3.12 (m, 2H), 2.84-2.77 (m, 2H), 2.63-2.56 (m, 2H), 2.56-2.46 (m, 1H), 2.24-1.65 (m, 23H); MS (ESI) calculated for $C_{39}H_{50}FN_3O_7$ $[M + H]^+$ m/z 692.37, found 692.34.

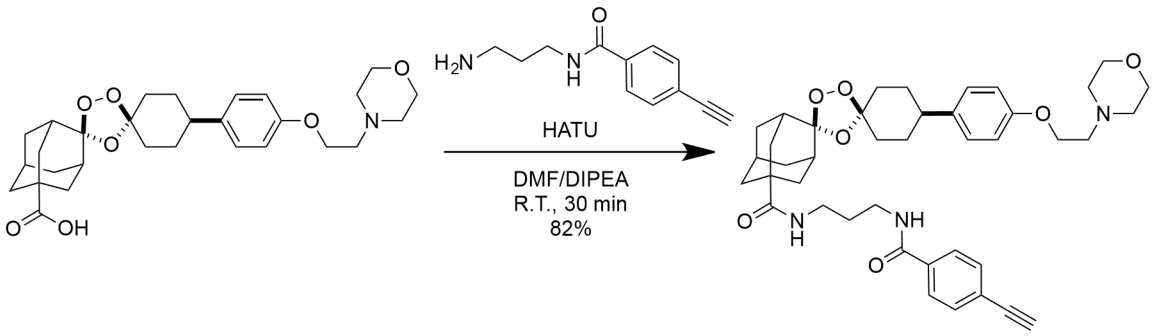

Scheme S2-3. Synthesis of HC_2-TRX

Synthesis of N-(3-(4-ethynlbenzamido)propyl)-4''-(4-(2-morpholinoethoxy)phenyl) dispiro[adamantane-2,3'-[1,2,4]trioxolane-5',1''-cyclohexane]-5-carboxamide (HC_2-TRX). To a round bottom flask containing a Teflon-coated magnetic stir bar under Ar(g) was added 4''(4-(2-morpholinoethoxy)phenyl)dispiro[adamantane-2,3'-[1,2,4]trioxolane-5',1''-cyclohexane]-5carboxylic acid (**6**, 50 mg, 0.1 mmol, 1.0 equiv.), HATU (56 mg, 0.1 mmol, 1.5 equiv.), N,N-diisopropylethylamine (0.068 ml, 0.4 mmol, 4 equiv.) and N,N-dimethylformamide (3 mL). To this stirring solution was added N-(3-aminopropyl)-4-ethynylbenzamide[4] (28 mg, 0.1 mmol, 1.2 equiv.) in one portion. The reaction was allowed to stir under argon for 30 minutes. At this point, the reaction was determined to be complete by LCMS. The crude reaction was purified by preparatory HPLC (Waters XBridge C18 column, 40-70% methanol/water with 0.05% formic acid) to afford N-(3-(4-

ethynlbenzamido)propyl)-4''-(4-(2-morpholinoethoxy)phenyl)dispiro[adamantane-2,3'-[1,2,4]trioxolane-5',1''-cyclohexane]-5-carboxamide **(HC_2-TRX)** as a white foam (56 mg, 82%). ^{1}H NMR (400 MHz, $CDCl_3$) δ (ppm) = 7.89 - 7.79 (m, 2H), 7.62 - 7.49 (m, 3H), 7.11 (d, *J* = 8.5 Hz, 2H), 6.82 (d, *J* = 8.8 Hz, 2H), 6.40 - 6.31 (m, 1H), 4.13 (t, *J* = 5.5 Hz, 2H), 3.83-3.69 (m, 4H), 3.48-3.30 (m, 4H), 3.24-3.16 (m, 1H), 2.87 (t, *J* = 5.5 Hz, 2H), 2.71-2.63 (m, 4H), 2.61 (s, 1H), 2.60-2.41 (m, 1H), 2.25-1.59 (m, 1H), ^{13}C NMR (100 MHz, $CDCl_3$) δ (ppm) = 178.1, 166.8, 156.8, 138.5, 134.3, 132.2, 127.6, 127.0, 125.1, 114.4, 110.1, 108.8, 82.8, 79.3, 66.4, 65.2, 57.4, 41.9, 40.9, 39.9, 39.5, 38.5, 36.7, 36.1, 36.0, 35.9, 35.6, 34.6, 33.6, 31.5, 29.8, 26.3; MS (ESI) calculated for $C_{41}H_{51}N_3O_7$ $[M + H]^+$ m/z 698.37, found 698.24.

REFERENCES

1. Poulos, T. L., Heme enzyme structure and function. *Chem Rev* **2014,** *114* (7), 3919-62.
2. Andrews, N. C., Iron homeostasis: insights from genetics and animal models. *Nature Reviews Genetics* **2000,** *1*, 208.
3. Kakhlon, O.; Cabantchik, Z. I., The labile iron pool: characterization, measurement, and participation in cellular processes. *Free Radical Biol. Med.* **2002,** *33* (8), 1037-1046.
4. Hider, R. C.; Kong, X., Iron speciation in the cytosol: an overview. *Dalton Trans* **2013,** *42* (9), 3220-9.
5. Johnson, D. C.; Dean, D. R.; Smith, A. D.; Johnson, M. K., Structure, Function, and Formation of Biological Iron-Sulfur Clusters. *Annu. Rev. Biochem.* **2005,** *74* (1), 247-281.
6. Bandyopadhyay, S.; Chandramouli, K.; Johnson, Michael K., Iron–sulfur cluster biosynthesis. *Biochem. Soc. Trans.* **2008,** *36* (6), 1112-1119.
7. James, S. A.; Roberts, B. R.; Hare, D. J.; de Jonge, M. D.; Birchall, I. E.; Jenkins, N. L.; Cherny, R. A.; Bush, A. I.; McColl, G., Direct in vivo imaging of ferrous iron dyshomeostasis in ageing Caenorhabditis elegans. *Chemical Science* **2015,** *6* (5), 2952-2962.
8. von Haehling, S.; Jankowska, E. A.; van Veldhuisen, D. J.; Ponikowski, P.; Anker, S. D., Iron deficiency and cardiovascular disease. *Nature Reviews Cardiology* **2015,** *12*, 659.

9. Wessling-Resnick, M., Iron Homeostasis and the Inflammatory Response. *Annu. Rev. Nutr.* **2010,** *30* (1), 105-122.

10. Manz, D. H.; Blanchette, N. L.; Paul, B. T.; Torti, F. M.; Torti, S. V., Iron and cancer: recent insights. *Ann. N. Y. Acad. Sci.* **2016,** *1368* (1), 149-161.

11. Torti, S. V.; Torti, F. M., Iron and cancer: more ore to be mined. *Nature Reviews Cancer* **2013,** *13*, 342.

12. Aron, A. T.; Reeves, A. G.; Chang, C. J., Activity-based sensing fluorescent probes for iron in biological systems. *Curr. Opin. Chem. Biol.* **2018,** *43*, 113-118.

13. Carter, K. P.; Young, A. M.; Palmer, A. E., Fluorescent Sensors for Measuring Metal Ions in Living Systems. *Chem Rev* **2014,** *114* (8), 4564-4601.

14. Petrat, F.; de Groot, H.; Rauen, U., Determination of the Chelatable Iron Pool of Single Intact Cells by Laser Scanning Microscopy. *Archives of Biochemistry and Biophysics* **2000,** *376* (1), 74-81.

15. Breuer, W.; Epsztejn, S.; Millgram, P.; Cabantchik, I. Z., Transport of iron and other transition metals into cells as revealed by a fluorescent probe. *American Journal of Physiology-Cell Physiology* **1995,** *268* (6), C1354-C1361.

16. Hirayama, T.; Okuda, K.; Nagasawa, H., A highly selective turn-on fluorescent probe for iron(II) to visualize labile iron in living cells. *Chemical Science* **2013,** *4* (3), 1250-1256.

17. Au-Yeung, H. Y.; Chan, J.; Chantarojsiri, T.; Chang, C. J., Molecular imaging of labile iron(II) pools in living cells with a turn-on fluorescent probe. *J Am Chem Soc* **2013,** *135* (40), 15165-73.

18. Spangler, B.; Morgan, C. W.; Fontaine, S. D.; Vander Wal, M. N.; Chang, C. J.; Wells, J. A.; Renslo, A. R., A reactivity-based probe of the intracellular labile ferrous iron pool. *Nat. Chem. Biol.* **2016,** *12*, 680.

19. Frangioni, J. V., In vivo near-infrared fluorescence imaging. *Curr. Opin. Chem. Biol.* **2003,** *7* (5), 626-634.

20. Ntziachristos, V., Going deeper than microscopy: the optical imaging frontier in biology. *Nat Meth* **2010,** *7* (8), 603-614.

21. Aron, A. T.; Heffern, M. C.; Lonergan, Z. R.; Vander Wal, M. N.; Blank, B. R.; Spangler, B.; Zhang, Y.; Park, H. M.; Stahl, A.; Renslo, A. R.; Skaar, E. P.; Chang, C. J., In vivo bioluminescence imaging of labile iron accumulation in a murine model of Acinetobacter baumannii infection. *Proceedings of the National Academy of Sciences* **2017,** *114* (48), 12669-12674.

22. Jacobson, O.; Kiesewetter, D. O.; Chen, X., Fluorine-18 Radiochemistry, Labeling Strategies and Synthetic Routes. *Bioconj. Chem.* **2015,** *26* (1), 1-18.

23. Ametamey, S. M.; Honer, M.; Schubiger, P. A., Molecular Imaging with PET. *Chem Rev* **2008,** *108* (5), 1501-1516.

24. Alauddin, M. M., Positron emission tomography (PET) imaging with (18)F-based radiotracers. *American Journal of Nuclear Medicine and Molecular Imaging* **2012,** *2* (1), 55-76.

25. Charman, S. A.; Arbe-Barnes, S.; Bathurst, I. C.; Brun, R.; Campbell, M.; Charman, W. N.; Chiu, F. C. K.; Chollet, J.; Craft, J. C.; Creek, D. J.; Dong, Y.; Matile, H.; Maurer, M.; Morizzi, J.; Nguyen, T.; Papastogiannidis, P.; Scheurer, C.; Shackleford, D. M.; Sriraghavan, K.; Stingelin, L.; Tang, Y.; Urwyler, H.; Wang, X.;

White, K. L.; Wittlin, S.; Zhou, L.; Vennerstrom, J. L., Synthetic ozonide drug candidate OZ439 offers new hope for a single-dose cure of uncomplicated malaria. *Proceedings of the National Academy of Sciences* **2011,** *108* (11), 4400-4405.

26. Tang, Y.; Dong, Y.; Wang, X.; Sriraghavan, K.; Wood, J. K.; Vennerstrom, J. L., Dispiro-1,2,4-trioxane analogues of a prototype dispiro-1,2,4-trioxolane: mechanistic comparators for artemisinin in the context of reaction pathways with iron(II). *J Org Chem* **2005,** *70* (13), 5103-10.
27. Ismail, H. M.; Barton, V. E.; Panchana, M.; Charoensutthivarakul, S.; Biagini, G. A.; Ward, S. A.; O'Neill, P. M., A Click Chemistry-Based Proteomic Approach Reveals that 1,2,4-Trioxolane and Artemisinin Antimalarials Share a Common Protein Alkylation Profile. *Angew Chem Weinheim Bergstr Ger* **2016,** *128* (22), 6511-6515.
28. Truillet, C.; Parker, M. F. L.; Huynh, L. T.; Wei, J.; Jami, K. M.; Wang, Y. H.; Shen, Y. S.; Sriram, R.; Wilson, D. M.; Kurhanewicz, J.; Evans, M. J., Measuring glucocorticoid receptor expression in vivo with PET. *Oncotarget* **2018,** *9* (29), 20399-20408.
29. Lazari, M.; Collins, J.; Shen, B.; Farhoud, M.; Yeh, D.; Maraglia, B.; Chin, F. T.; Nathanson, D. A.; Moore, M.; van Dam, R. M., Fully Automated Production of Diverse 18F-Labeled PET Tracers on the ELIXYS Multireactor Radiosynthesizer Without Hardware Modification. *Journal of Nuclear Medicine Technology* **2014,** *42* (3), 203-210.

30. Moehrle, J. J.; Duparc, S.; Siethoff, C.; Giersbergen, P. L. M.; Craft, J. C.; Arbe-Barnes, S.; Charman, S. A.; Gutierrez, M.; Wittlin, S.; Vennerstrom, J. L., First-in-man safety and pharmacokinetics of synthetic ozonide OZ439 demonstrates an improved exposure profile relative to other peroxide antimalarials. *British Journal of Clinical Pharmacology* **2012,** *75* (2), 535-548.

31. Lauterwasser, E. M.; Fontaine, S. D.; Li, H.; Gut, J.; Katneni, K.; Charman, S. A.; Rosenthal, P. J.; Bogyo, M.; Renslo, A. R., Trioxolane-Mediated Delivery of Mefloquine Limits Brain Exposure in a Mouse Model of Malaria. *ACS Med Chem Lett* **2015,** *6* (11), 1145-9.

Chapter 3: An Fe(II)-reactive prodrug strategy selectively delivers MEK inhibitors to KRAS-driven cancers while mitigating known clinical toxicities.

Muir, R.K., Jiang, H., Gonciarz, R.L., Renslo, A.R., Collisson, E. A.

INTRODUCTION

The field of oncology is progressively moving closer to the ideal of "personalized medicine," in which weaknesses in a patient's cancer are identified and exploited with a matching chemotherapy.[1,2] For example, patients identified as having mutations in the MAP kinase pathway will be administered MEK inhibitors to stop the aberrant signaling pathway. While these targeted therapeutics can show remarkable antitumor activity, many times they carry significant side-effects in the clinic due to on-target, off-tissue activity. In the case of patients administered MEK inhibitors, these drugs are known to cause serious skin rashes and ocular toxicities in 10-20% of patients, often limiting the dosing regimen.[3] This suggests MEK inhibitors as a candidate for a prodrug strategy as a method to mitigate on-target, off-tissue activity *in vivo*.

The Renslo lab has recently reported an Fe(II)-activated prodrug platform that can selectively deliver amine-bearing payloads to cancer cells with an elevated labile iron pool (LIP).[4] However, little information is known clinically about what oncogenic drivers or cancer subtypes are associated with an elevated LIP. While nodes of iron metabolism regulation are generally highly regulated in healthy tissues, various cancers have been noted to alter expression levels in this pathway indicating an increased avidity for iron.[5,6] Many cancers have been observed to upregulate transferrin receptor

levels, though no clear connection between this upregulation and oncogenic driver or cancer subtype has been clearly established. Here we hypothesize that oncogenic mutations of KRAS are connected to this elevated LIP, and that we can leverage this as a method to selectively deliver MEK inhibitors to KRAS-driven cancers while mitigating known on-target, off-tissue toxicities.

RESULTS AND DISCUSSION

PET/CT imaging of ^{68}Ga accumulation in cancers bearing KRAS mutations

As 97% of patients with pancreatic ductal adenocarcinoma (PDAC) harbor a KRAS mutation as their primary oncogenic driver,[7,8] we hypothesized these tumors would have an upregulated transferrin receptor level. Through PET/CT imaging, a metastasis originating from PDAC can be seen to accumulate ^{68}Ga and readily identified by PET/CT imaging (Fig 3-1A). To further investigate this link between KRAS-driven cancers and increased avidity for iron, we performed several preclinical PET/CT imaging studies. Mice bearing xenografts with wild type KRAS expression or with oncogenic KRAS mutations were injected with ^{68}Ga-loaded transferrin. Those bearing a KRAS mutation accumulate significantly more of this Fe(III) mimetic than other xenografts (Fig 3-1B), suggesting KRAS mutations play a role in altering iron metabolism.

KRAS mutation increases the reactive Fe(II) pool in cells

While the PET/CT imaging studies suggest an increased avidity for Fe(III) in KRAS-driven cancers, it does not inform on aberrant levels of reactive Fe(II) found in the labile

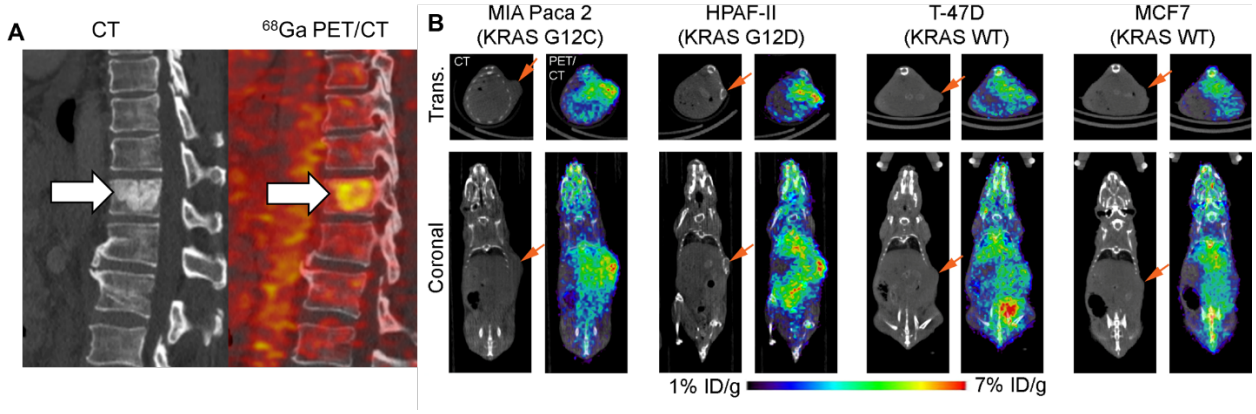

Figure 3-1: **a)** PET imaging with ^{68}Ga (an Fe^{3+} mimetic) detects a bone metastasis from a patient with pancreatic ductal adenocarcenoma. **b)** ^{68}Ga PET imaging of mice bearing xenografts with wild type or mutant KRAS. Tumors bearing an oncogenic KRAS mutation have an increased avidity for ^{68}Ga, indicating an elevated level of transferrin receptor.

iron pool (LIP). To assess the effect of KRAS mutations on the LIP, mouse fibroblasts were transfected with TGT-hKRAS-G12D and treated with FerroFar Red, a probe for labile Fe(II).[9] A significantly elevated Fe(II) pool can be detected 72 hour post-transfection (Fig 3-2A), around the same time these cells reached maximum expression of mutant KRAS (Fig 3-2B). This finding was confirmed with an orthogonal Fe(II) probe, TRX-PURO (Fig 3-2D),[10] suggesting a single mutation to KRAS can significantly alter the cellular labile iron pool.

The concentration of the labile iron pool was then determined in a panel of cancer cell lines with FerroFar Red. Notably, the pancreatic cancer cell lines bearing KRAS mutations had approximately 10X more reactivity with the probe than the breast cancer cell lines with wild type KRAS expression (Fig 3-2E). This data in combination with the PET/CT imaging experiment suggest that KRAS is altering the cellular iron metabolism to increase both the cells avidity for Fe(III) and an elevated intracellular labile iron pool.

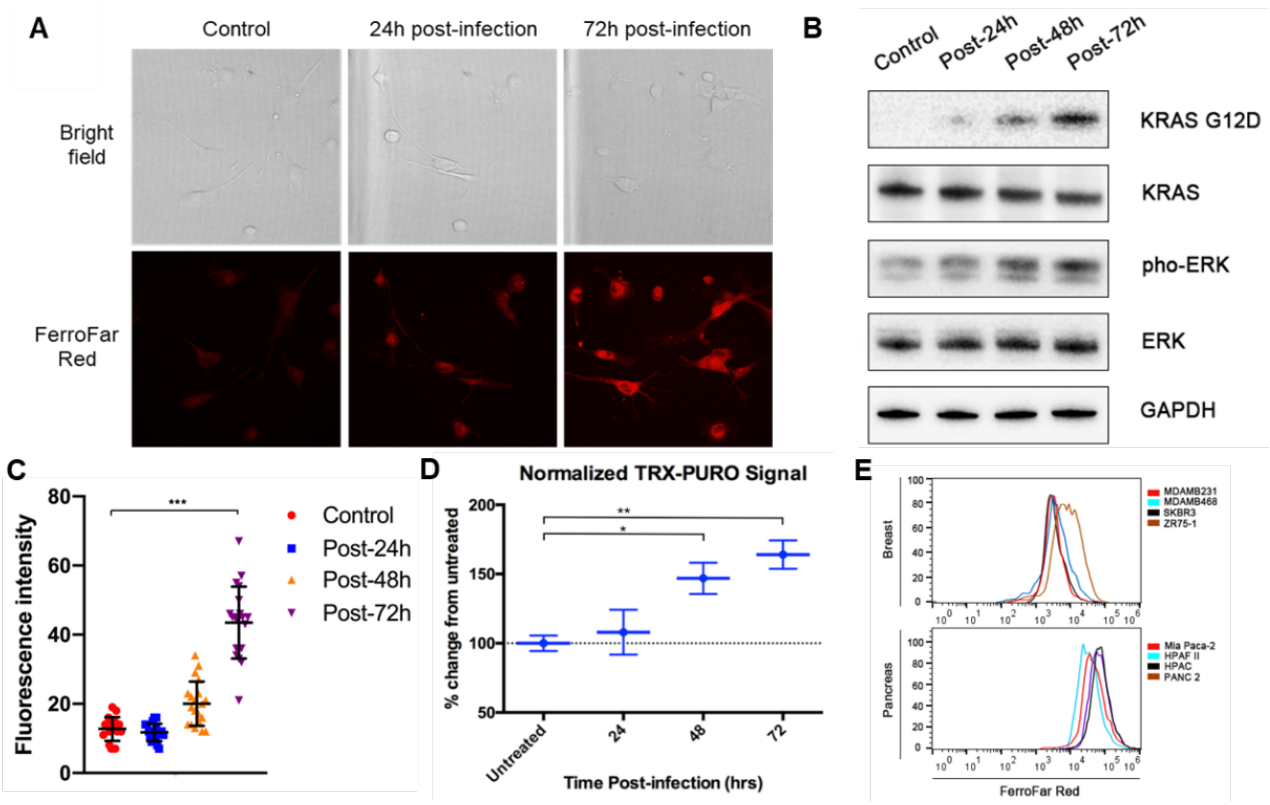

Figure 3-2 **a)** Mouse fibroblasts were transfected with TGT-hKRAS-G12D. Fe(II) concentration was monitored through SiRhoNox **b)** Transfection was confirmed via Western Blot. Both an increase in KRAS G12D as well as pERK can be observed over 72 hours. **c)** Quantification of transfected fibroblasts treated with SiRhoNox. An increase in Fe(II) can be observed by 72 hours post-transfection. **d)** An elevated Fe(II) pool in KRAS-transfected cells was confirmed with TRX-PURO, an alternative Fe(II)-specific probe. **e)** The Fe(II) levels were determined in various breast and pancreatic cancer cell lines via flow cytometry after treatment with SiRhoNox. All pancreatic cancer cell lines appear to have more Fe(II) than breast.

The elevated labile pool in KRAS-driven pancreatic cancers can be exploited by an Fe(II)-activated prodrug strategy

There are several pharmacological examples of leveraging an elevated labile iron pool.[5] The Renslo lab has historically leveraged the Fe(II) reactivity of 1,2,4-trioxolanes (TRX) as a method to selectively deliver amine-containing payloads to areas of elevated ferrous iron.[11,12] Previous work has focused on delivering bulk cytotoxins in these cancer cells. In this work, we explore the idea of coupling a targeted therapeutic in

Cobimetinib, a clinically approved MEK inhibitor with serious clinical toxicities. Cobimetinib readily reacts with our previously described coupling conditions to generate a trioxolane-caged Cobimetinib (TRX-COBI, Fig 3-3B).

When introduced to several pancreatic cancer cell lines, TRX-COBI demonstrates sufficient uncaging and subsequent MEK inhibition by Western blot (Fig 3-3C). The antitumor activity of TRX-COBI was then tested across a panel of breast and pancreatic cancer cell lines. A TRX-COBI susceptibility ratio was obtained by normalizing the GI_{50} of TRX-COBI to that of parent Cobimetinib. Interestingly, each pancreatic cancer cell line was more susceptible to TRX-COBI than any of the breast cancer lines, consistent with the elevated reactive Fe(II) pool observed with FerroFar Red.

TRX-COBI shows equivalent MEK inhibition and antitumor activity as parent Cobimetinib across several preclinical models

The MEK inhibition and antitumor activity of TRX-COBI was then assessed *in vivo*. Mice bearing KRAS-driven xenografts or PDX models were treated with equimolar doses of Cobimetinib or TRX-COBI for 20 days. TRX-COBI shows similar MEK inhibition (Fig 3-4A) and growth inhibition (Fig 3-4B) as parent Cobimetinib. This trend holds true in more clinically-relevant models as well. First the efficacy of TRX-COBI was examined in PDAC.fLuc (*Kras*^{G12D}) mice. These mice bear KRAS-driven xenografts implanted in the pancreas which more accurately represents the pancreatic cancer tumor environment. While tumor volume cannot be monitored with calipers due to the xenograft location, it can be estimated by monitoring luciferase activity. Significant tumor growth inhibition is be observed after 20 days of dosing with equimolar COBI or TRX-COBI (Fig 3-4C). This

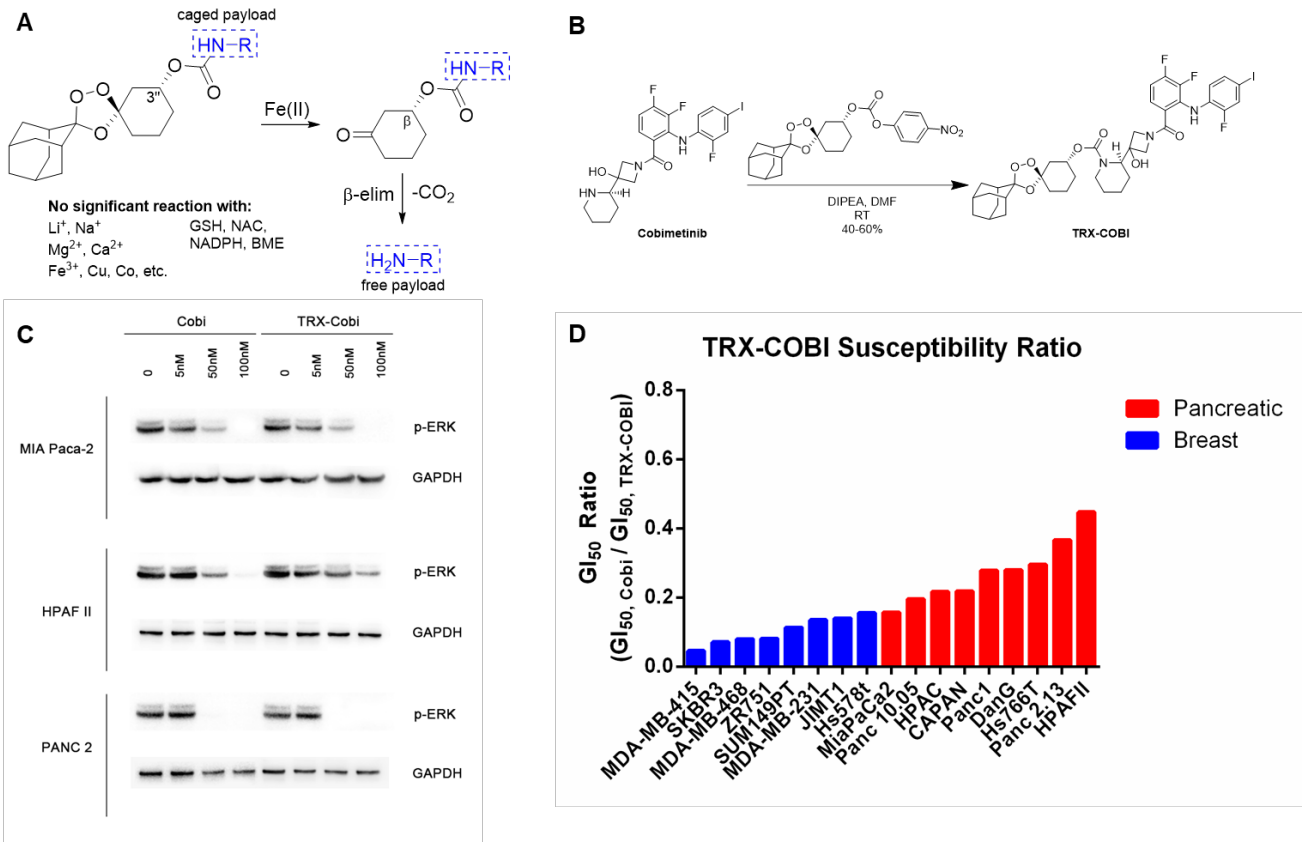

Figure 3-3: **a)** A general reaction mechanism of TRX-based prodrugs to afford traceless release of amine-containing payloads upon reaction with Fe(II). **b)** TRX-COBI can be readily synthesized by reacting parent Cobimetinib with previously reported TRX-PNP. **c)** Three pancreatic cancer cell lines were dosed with either Cobimetinib (COBI) or TRX-COBI for 6 hours. On-target inhibition of MEK can be observed by Western blot. **d)** A panel or breast and pancreatic cancer cells were dosed with COBI and TRX-COBI for 72 hours. The GI_{50} of TRX-COBI for each cell was normalized to that of parent COBI to generate a TRX susceptibility ratio.

is further confirmed by reduced tumor weight determined after death (Fig 3-4D).

This experiment was then repeated in KPT mice (*Kras*$^{LSLG12D/+;}$ *p53*$^{flox/flox}$*; R26*$^{tdTomato/+}$), often considered the "gold standard" preclinical model in the field of KRAS-driven cancer.[13] Dosing began 20 days after intratracheal administration of Ad-CRE and continued daily for 60 days. Mice treated with equimolar doses of Cobimetinib and TRX-COBI showed considerable growth inhibition of the tumor compared to vehicle treated

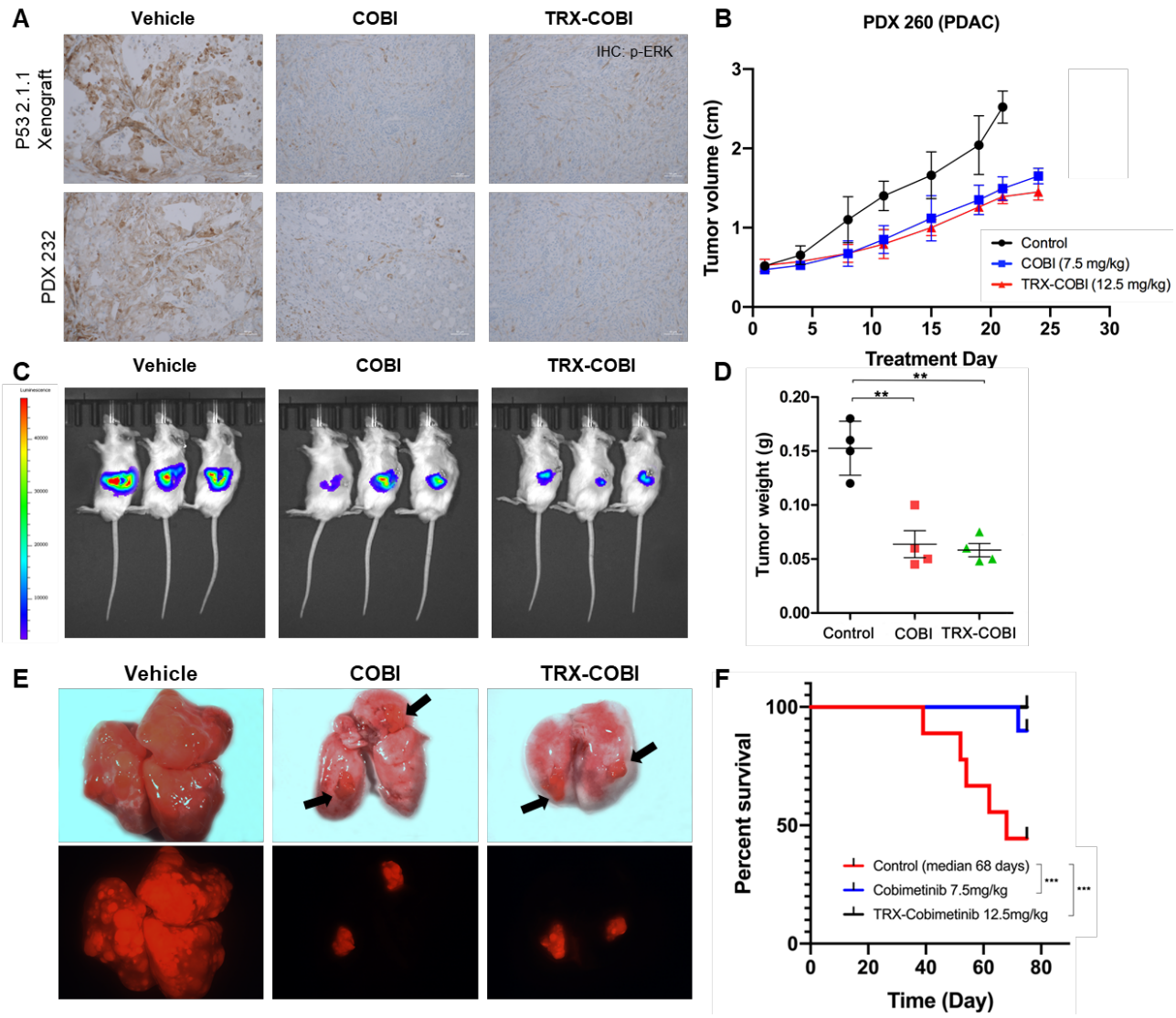

Figure 3-4: **a)** Tissue slices of tumors taken from mice treated with either Cobimetinib (COBI, 7.5 mg/kg), TRX-COBI (12.5 mg/kg) or vehicle. On-target inhibition of MEK is visualized by staining for pERK via immunohistochemistry. **b)** TRX-COBI has similar antitumor activity of an equimolar dose of COBI in a KRAS-driven PDX model. **c)** Mice bearing p53.luc tumors after 15 days of dosing with COBI (7.5 mg/kg), TRX-COBI (12.5 mg/kg) or vehicle. Tumor volume can be measured by luminescence. **d)** Tumors of the mice from **c** were excised and weighed. TRX-COBI again maintains similar antitumor activity to parent Cobimetinib. **e)** Excised lungs from KPT mice after 60 days of dosing. TRX-COBI and COBI greatly reduce tumor growth. **f)** Kaplan-Meier survival curve of mice from **e** (n=10 per arm).

mice (Fig 3-4E). Interestingly, all mice dosed with TRX-COBI survived the duration of the study (Fig 3-4F) while showing negligible adverse reactions to the treatment.

Known on-target off-tissue toxicities of MEK inhibitors are mitigated by TRX-COBI

As mentioned previously, MEK inhibitors used in the clinic carry severe side-effects, most significantly in the skin (rash) and eyes (chorioretinopathy). These are now known to be the result of on-target yet off-tissue activity, meaning Cobimetinib is inhibiting normal MAPK signaling in these tissues. These tissues are not known to have an aberrant iron metabolism, so it would be expected that TRX-COBI would remain fully caged and inactive in these areas of known clinical toxicity.

The MEK inhibition of TRX-COBI was assessed in retinal pigment epithelia cells (RPE-1) and keratinocytes (HaCaT). Strikingly, TRX-COBI shows highly reduced MEK inhibition in these cells when compared to Cobimetinib (Fig 3-5a), indicating a lack of TRX-fragmentation and uncaging. In preclinical models, MEK inhibitors are known to cause a reduction in the epidermal layer.[14] Tail samples were collected from mice dosed with TRX-COBI (12.5 mg/kg), Cobimetinib (7.5 mg/kg) or vehicle for 20 days and the epidermal thickness was determined. While mice dosed with Cobimetinib showed significant reduction in epidermal layer, remarkably those mice dosed with TRX-COBI showed no statistical difference compared to those dosed with vehicle. This data combined with the mitigated *in vitro* activity suggests the clinical on-target off-tissue toxicities of Cobimetinib are sufficiently caged by dosing with TRX-COBI.

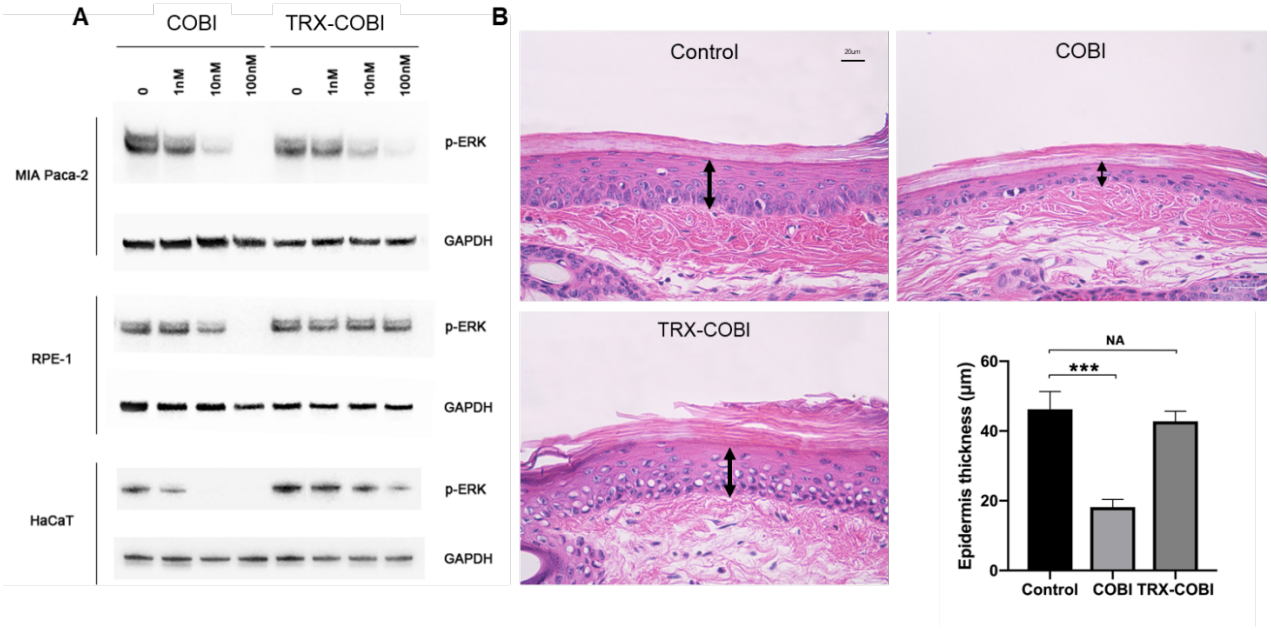

Figure 3-5: Caged on-target off-tissue activity of TRX-COBI. **a)** Western blot showing caged MEK-inhibition of TRX-COBI in retinal pigment epithelial (RPE-1) and keratinocyte (HaCaT) cell lines while maintaining on-target inhibition in a pancreatic cancer cell line (Mia-Paca-2). **b)** Representative tissue slices of mouse tails dosed with COBI (7.5 mg/kg), TRX-COBI (12.5 mg/kg), or vehicle. Prolonged MEK inhibition causes a reduction of epidermal thickness as observed in mice treated by COBI. Quantification shows no statistical difference between mice treated with TRX-COBI and vehicle (n=5 per arm).

CONCLUSIONS AND FUTURE DIRECTIONS

Here we report utilizing the TRX-prodrug platform to selectively deliver Cobimetinib, a clinically approved MEK inhibitor, to KRAS-driven cancers. TRX-COBI shows similar on-target activity and growth inhibition to parent Cobimetinib across several pancreatic cancer cell lines. This trend holds true across several preclinical models, including the "gold standard" KPT model. Pleasingly, TRX-COBI shows masked activity in areas of known clinical toxicities caused by on-target, off-tissue activity both *in vitro* and *in vivo*.

The major future direction of this project is to use TRX-COBI in combination with other chemotherapies for which Cobimetinib could not be used. For example, PI3K inhibitors

have long been desired to be used in combination with MEK inhibitors as tumors primarily driven by one of these pathways will often “escape” targeted therapeutics through the other pathway. However, combining PI3K and MEK inhibitors have proven to carry too severe side-effects to be used effectively in the clinic. By caging the off-tissue toxicities of a MEK inhibitor, we hypothesize TRX-COBI could be used safely in combination with PI3K inhibitors. Preclinical studies are currently being performed to test this hypothesis.

MATERIALS AND METHODS

Cell Line and Cell Culture

Cells were maintained in an atmosphere of 5% CO2 in RPMI 1640 or DMEM media purchased from HyClone supplemented with 10% FBS (Gibco) and Pen/Strep (1× final concentration, Gemini BioProducts).

In vitro inhibition

In vitro inhibition was determined using the HDAC-Glo I/II screening system (Promega). Compounds were dissolved in DMSO then diluted in buffer to give a final concentration of 0.1% DMSO. Signal was read using the Flexstation 3 (Molecular Devices)

Western Blots

Cells were plated in 6-well plate at 10^6 cells per well and incubated for at least 24 h prior to exposure to compounds. Cells were then treated with specified concentrations of compound that resulted in a final concentration of 0.1% DMSO. After the specified amount of time, cells were pelleted by centrifuging at 200 x g for 5 minutes. Cell pellets were washed with PBS and then lysed with mPER lysis buffer (Thermo Fisher) containing protease inhibitor cocktail (1x concentration, Sigma). Protein concentration was determined using Pierce BCA assay (Thermo Fisher). Samples were normalized to 20 µg per well and run on a 4-12% Bis-Tris Protein Gel (Thermo Fisher). Transfer and blotting was performed using the iBlot 2 and iBind system (Thermo Fisher).

Cell toxicity assay

Cells were plated in 96-well Greiner black µClear tissue culture plates at 10^4 cells per well for at least 24 h prior to exposure to compounds. Cells were then treated in triplicate with escalating concentrations of compound performed in media containing a final concentration of 0.1% DMSO and 200 µL of media per well. Cell viabilities were determined 72 h after treatment by Cell-Titer Glo assay (Promega) on the Flexstation 3 reader (Molecular Devices). Relative luminescent units (RLU) were plotted against corresponding drug concentrations and fitted with a standard four-parameter sigmoidal curve with GraphPad Prism 6. Data reported at the IC50, and error bars represent SEM (n = 3).

Pharmacokinetic Assays

NSG mice were administered a single IP dose of TRX-COBI (12.5 mpk, n=3). Blood was collected at indicated timepoints and from which drug concentrations were determined by Integrated Analytical Solutions, Inc (Berkeley, CA).

Other

Graphing and analysis of data were done using GraphPad Prism 6 software and Microsoft Excel 2010. Figures were prepared with Microsoft Powerpoint and Adobe Design Standard CS6 software.

SUPPLEMENTAL INFORMATION

General Information

All reactions were performed under an Argon atmosphere using anhydrous solvents obtained from commercial suppliers in oven-dried round-bottom flasks containing Teflon coated stirrer bars, unless otherwise noted. All anhydrous solvents used were purchased from Sigma-Aldrich and used without further purification. Solvents to be employed in flash column chromatography and reaction work-up procedures were purchased from either Sigma-Aldrich or Fisher Scientific. All other reagents were obtained commercially and used without further purification, unless otherwise stated. Air and/or moisture sensitive reagents were transferred via syringe and were introduced into reaction vessels through rubber septa. Reactions were monitored using thin layer

chromatography (TLC), performed on 0.25-mm EMD pre-coated glass-backed silica gel 60 F-254 plates. Column chromatography was performed on Silicycle Sili-prep cartridges using a Biotage Isolera Four automated flash chromatography system. Compounds were visualized under UV light or through staining with permanganate, iodine, or most preferably for trioxolane analogs, Seebach's "Magic" stain (composed of the following: 2.5 g phosphomolybdic acid, 1.0 g cerium sulfate, 6 mL concentrated sulfuric acid, and 94 mL water). Solutions containing crude reaction mixtures, as well as those obtained upon reaction work-up, and chromatography fractions were first concentrated by rotary evaporation at temperatures under 40 ˚C, at 20 Torr then subsequently placed under Hi-Vac at 0.5 Torr unless otherwise indicated.

Instrumentation

NMR spectra were recorded on either a Varian INOVA 400 MHz spectrometer (with 5 mm Quad-Nuclear Z-Grad Probe), or a Bruker AvanceIII HD 400 MHz (with 5mm BBFO Z-gradient Smart Probe), calibrated to $CH(D)Cl_3$ as an internal reference (7.26 and 77.00 ppm for ^{1}H and ^{13}C NMR spectra, respectively). Data for ^{1}H NMR spectra are reported in terms of chemical shift (δ, ppm), multiplicity, coupling constant (Hz), and integration. Data for ^{13}C NMR spectra are reported in terms of chemical shift (δ, ppm), with multiplicity and coupling constants in the case of C–F coupling. The following abbreviations are used to denote the multiplicities: s = singlet; d = doublet; dd = doublet of doublets; dt = doublet of triplets; dq = doublet of quartets; ddd = doublet of doublet of doublets; t = triplet; td = triplet of doublets; tt = triplet of triplets; q = quartet; qd = quartet of doublets; quin = quintet; sex = sextet; m = multiplet. LC-MS and compound purity

were determined using Waters Micromass ZQ 4000, equipped with a Waters 2795 Separation Module, Waters 2996 Photodiode Array Detector, and a Waters 2424 ELSD. Separations were carried out with an XBridge BEH C18, 3.5μm, 4.6 x 20 mm column, at ambient temperature (unregulated) using a mobile phase of water-methanol containing a constant 0.1 % formic acid.

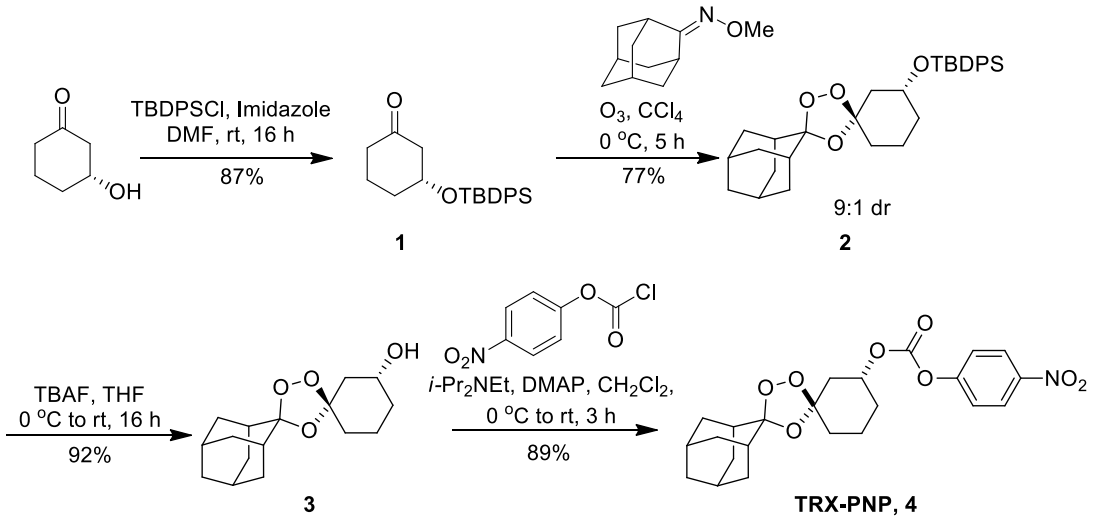

Scheme S3-1: Synthesis of TRX-PNP

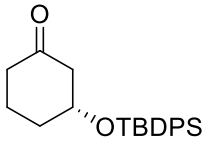

(*R*)-3-((*tert*-butyldiphenylsilyl)oxy)cyclohexan-1-one (1). A 200-mL RBF equipped with a stirbar, rubber septum, and argon inlet was charged with (*R*)-3-hydroxycyclohexan-1-one[15] (2.1 g, 18.4 mmol, 1.0 equiv), N,N-dimethylformamide (40 mL), and imidazole (2.51 g, 36.8 mmol, 2.0 equiv). The mixture was cooled at 0 °C while *tert*-butyl(chloro)diphenyl silane (5.3 mL, 20.2 mmol, 1.1 equiv) was added dropwise via syringe. The reaction mixture was allowed to slowly warm to room temperature. After stirring for 16 h, the reaction was deemed to be incomplete based on

TLC and LCMS analysis. The reaction mixture was then diluted with 100 mL of EtOAc and 100 mL H_2O. The organic phase was separated and washed with two 50 mL portions of brine, dried over $MgSO_4$, filtered, and concentrated to afford a colorless oil. The residue was purified through flash column chromatography (330 g silica gel cartridge, 0–20% EtOAc/Hexanes, product eluted during 8% EtOAc/Hex) to yield the product (6.01 g, 93%) as a colorless oil. ^{1}H NMR (400 MHz, CHLOROFORM-*d*) δ 1.08 - 1.12 (s, 9 H), 1.64 - 1.71 (m, 1 H), 1.78 - 1.83 (m, 2 H), 2.17 (br dd, *J*=8.46, 5.78 Hz, 1 H), 2.25 - 2.32 (m, 1 H), 2.35 - 2.42 (m, 1 H), 2.47 (d, *J*=4.99 Hz, 2 H), 4.23 (t, *J*=4.93 Hz, 1 H), 7.39 - 7.49 (m, 6 H), 7.68 - 7.72 (m, 4 H); ^{13}C NMR (100 MHz, CHLOROFORM-*d*) δ 19.2, 20.6, 26.6, 26.9, 32.9, 41.2, 50.4, 71.1, 127.69, 127.72, 129.8, 129.9, 133.6, 133.9, 134.9, 135.7, 135.8, 210.0; MS (ESI) calculated for $C_{22}H_{29}O_2Si$ $[M + H]^+$ *m/z* 353.19, found 353.46.

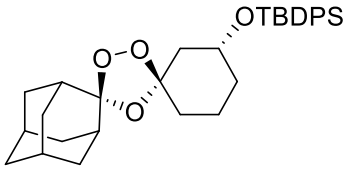

(1*R*,3*R*)-*tert*-butyl((dispiro[adamantane-2,3'-[1,2,4]trioxolane-5',1''-cyclohexan]-3''-yl)oxy)diphenylsilane (2). A 200-mL recovery flask was charged with silyl ketone, 1 (1.51 g, 4.28 mmol, ca. 1 equiv), carbon tetrachloride (100 mL), and *O*-methyl 2-adamantanone oxime[2] (768 mg, 4.28 mmol, 1 equiv). This solution was then cooled to 0 ˚C and subsequently sparged with O_2 for 10 minutes. The reaction was kept at 0 ˚C while ozone was bubbled (2 L/min, 40% power) through the solution. After stirring for 90 mins, the reaction was deemed to be incomplete based on TLC and LCMS analysis and additional oxime (0.386 g, 2.14 mmol, 0.5 equiv) was added in a single portion to the

reaction. Additionally, carbon tetrachloride (50 mL) was added to the solution. Ozone was bubbled through the reaction for another 45 mins, the LCMS indicated the ratio of pruduct formation: silyl ketone was 2:1. Another 0.5 eq of oxime (0.386 g, 2.14 mmol, 0.5 equiv) was added in a single portion to the reaction, and ozone was bubbled through the reaction for another 45 mins, at which point the reaction was determined to be complete based on LCMS and TLC analysis. The solution was then purged with O_2 for 10 minutes in an effort to remove any dissolved ozone, followed by sparging with argon gas for 10 minutes to remove any dissolved oxygen. The solution was then concentrated under reduced pressure to provide an extremely viscous oil. The residue was purified through flash column chromatography (120 g silica gel cartridge, 0–20% EtOAc/Hexanes, product eluted during 5% EtOAc/Hex) to yield product (2.01 g, 91%) as a white foamy solid. The diastereoselectivity of the Griesbaum coozonolysis was determined to be 12:1 in favor of the *trans* diastereomer. ^{1}H NMR (400 MHz, CHLOROFORM-*d*) δ 1.08 (s, 9 H), 1.19 - 1.36 (m, 3 H), 1.46 - 1.65 (m, 3 H), 1.65 - 1.84 (m, 12 H), 1.95 - 2.05 (m, 3 H), 3.78 - 3.85 (m, 1 H), 3.89 - 3.96 (m, 1 H), 7.36 - 7.46 (m, 6 H), 7.69 (td, *J*=7.67, 1.46 Hz, 4 H); ^{13}C NMR (100 MHz, CHLOROFORM-*d*) δ 19.2, 19.9, 26.5, 26.9, 27.0, 33.2, 33.8, 34.4, 34.8 ,36.2, 36.3, 36.8, 43.8, 69.8, 109.2, 111.2, 127.5, 127.6, 129.5, 129.6, 134.4, 134.5, 135.75, 135.78; MS (ESI) calculated for $C_{32}H_{42}NaO_4Si$ $[M + Na]^+$ *m/z* 541.28, found 541.56.

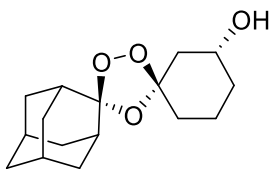

(1*R*,3*R*)-Dispiro[cyclohexane-1,3'-[1,2,4]trioxolane-5',2''-tricyclo[3.3.1.1^{3,7}]decan]-3-ol (3).

To a stirred solution of **2** (2.0 g, 3.86 mmol, 1 equiv) in THF (20 mL) was added a solution of tetrabutylammonium fluoride (1.0 M in THF, 19.2 ml, 19.3 mmol, 5 equiv) dropwise to this solution while stirring at 0 °C. The reaction mixture was left to warm slowly to room temperature and stirred for 12 h, at which point it was determined to be complete based on TLC and LCMS analysis. The reaction was then diluted with brine (100 mL) and extracted with EtOAc (100 mL x 2). The organic layer was then dried over anhydrous Na_2SO_4, filtered, and concentrated under reduced pressure to afford a yellow oil. The residue was then purified through flash column chromatography (80 g silica gel cartridge, 0–50% EtOAc/Hexanes, product eluted during 20% EtOAc/Hexanes) to yield the product (1.01 g, 93%) as a white powder: ^{1}H NMR (400 MHz, CHLOROFORM-*d*) δ 1.47 - 1.63 (m, 2 H), 1.69 - 1.88 (m, 12 H), 1.90 - 2.05 (m, 7 H), 2.07 (d, *J*=4.02 Hz, 1 H), 2.47 (br s, 1 H), 3.94 - 4.14 (m, 1 H); ^{13}C NMR (100 MHz, CHLOROFORM-*d*) δ 19.1, 26.4, 26.8, 33.1, 33.8, 34.7, 34.8, 34.9, 34.9 , 36.2, 36.2, 36.7, 41.7, 67.9, 109.1, 111.9; MS (ESI) calculated for $C_{16}H_{24}O_4$ $[M + H]^+$ *m/z* 281.17, found 281.51.

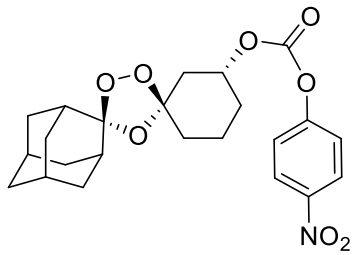

(1*R*,3*R*)-3-(*p*-Nitrophenoxycarbonyloxy)dispiro[cyclohexane-1,3'-[1,2,4]trioxolane-5',2''-tricyclo[3.3.1.1^{3,7}]decane] (4). To an oven-dried round bottom flask containing a

magnetic stir bar under an Ar(g) atmosphere was added alcohol **3** (0.150 mg, 0.54 mmol, 1.0 equiv) dissolved in dichloromethane (10 mL), N,N-diisopropylethylamine (0.30 mL, 1.74 mmol, 3.25 equiv), and 4-dimethylaminopyridine (0.078 g, 0.64 mmol, 1.2 equiv). The mixture was cooled to 0 °C while 4-nitrophenyl chloroformate (0.350 g, 1.74 mmol, 3.25 equiv) was added as a solid in two portions. The solution was allowed to stir at room temperature for 3 hours. The reaction was then diluted with DI H_2O (100 mL) and subsequently extracted with EtOAc (100 mL). The organic layer was washed repeatedly by potassium carbonate solution until the aqueous layer was colorless and no longer yellow (meaning that all of the *p*-nitrophenol had been successfully removed from the organic layer). The organic layer was dried over anhydrous Na_2SO_4, filtered, and concentrated under reduced pressure to yield thick yellow oil. The residue was then purified through flash column chromatography (80 g silica gel cartridge, 0–25% EtOAc/Hexanes, product eluted during 10% EtOAc/Hex) to yield the desired product (208 mg, 87%) as a pale yellow oil (93:7 dr). ^{1}H NMR (400 MHz, CHLOROFORM-*d*) δ 8.26 (d, *J*=9.13 Hz, 2 H), 7.38 (br d, *J*=9.13 Hz, 2 H), 4.94 (td, *J*=9.19, 4.50 Hz, 1 H, minor diastereomer), 4.79 - 4.88 (m, 1 H), 2.32 - 2.42 (m, 1 H), 2.10 (br d, *J*=8.77 Hz, 1 H), 1.69 - 2.00 (m, 1 H), 1.64 - 2.01 (m, 17 H), 1.40 - 1.64 (m, 3 H), 1.20 - 1.28 (m, 1 H), 0.83 - 0.96 (m, 1 H); ^{13}C NMR (100 MHz, CHLOROFORM-*d*) δ 19.5, 26.4, 26.8, 30.0, 33.5, 34.7, 34.7, 34.7, 34.8, 36.3, 36.3, 36.7, 39.5, 76.2, 108.3, 111.9, 121.7,121.9,125.3,145.3,151.6, 155.5; MS (ESI) m/z [M+H]+ calcd for $C_{23}H_{27}NNaO_8$: 468.16; found 467.99.

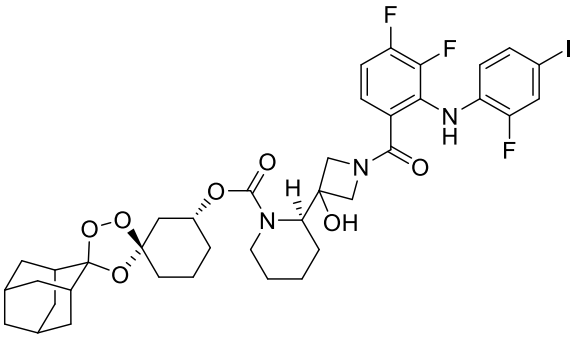

(3''R,4'R)-dispiro[adamantane-2,2'-[1,2,4]trioxolane-4',1''-cyclohexan]-3''-yl (2R)-2-(1-{3,4-difluoro-2-[(2-fluoro-4-iodophenyl)amino]benzoyl}-3-hydroxyazetidin-3-yl)piperidine-1-carboxylate (TRX-COBI). To an oven-dried round bottom flask containing a magnetic stir bar under an Ar(g) atmosphere was added Cobimetinib (0.150 mg, 0.28 mmol, 1 eq) and TRX-PNP **4** (0.150 mg, 0.34 mmol, 1.2 equiv) dissolved in dimethylformamide (10 mL), N,N-diisopropylethylamine (0.30 mL, 1.74 mmol, 6 equiv), and 4-dimethylaminopyridine (0.038 g, 0.34 mmol, 1.2 equiv). The solution was allowed to stir at room temperature for 3 hours to 72 hours, monitoring reaction progress by LCMS. The reaction was then diluted with DI H_2O (100 mL) and subsequently extracted with EtOAc (100 mL). The organic layer was washed repeatedly with a satd. sodium bicarbonate solution until the aqueous layer was colorless and no longer yellow. The organic layer was dried over anhydrous Na_2SO_4, filtered, and concentrated under reduced pressure to yield thick yellow oil. The residue was then purified through flash column chromatography (40 g silica gel cartridge, 0–50% EtOAc/Hexanes, 0-15% MeOH + 0.7N NH_3/DCM, product eluted during 40% EtOAc/Hex, unreacted Cobimetinib eluted during 15% MeOH + 0.7N NH_3) to yield the desired product (30-50%) as a white solid. ^{1}H NMR (1H NMR (400 MHz, CDCl3) δ 8.60 (br s, 1 H), 8.41 (br s, 1 H), 7.39 (dd, J = 10.4, 1.6 Hz, 1 H), 7.31 - 7.34 (m, 1 H), 7.32

(d, J = 8.5 Hz, 1 H), 7.15 (br s, 1 H), 6.82 (app q, J = 1.0 Hz, 1 H), 6.61 (app td, J = 8.5, 5.6 Hz, 1 H), 5.45 (br s, 1 H), 4.88 (br s, 1 H, minor diastereomer), 4.76 (app spt, J = 1.0 Hz, 1 H), 4.11 - 4.25 (m, 2 H), 3.93 - 4.11 (m, 3 H), 3.22 - 3.44 (m, 1 H), 2.87 (br s, 1 H), 2.07 - 2.25 (m, 1 H), 1.86 - 2.02 (m, 8 H), 1.72 - 1.85 (m, 7 H), 1.46 - 1.65 (m, 6 H), 1.21 - 1.46 (m, 3 H); 13C NMR (100 MHz, CDCl3) δ 169.1, 155.4, 154.4 (d, J = 248.7), 153.0 (d, J = 253.1), 152.6 (d, J = 252.4), 143.5 (d, J = 250.2), 143.4 (br d, J = 250.2), 142.2, 132.9 (d, J = 3.7 Hz), 132.6 (br d, J = 3.7 Hz) 130.8 (br d, J = 10.3 Hz), 124.3 (d, J = 21.3 Hz), 119.9, 119.6, 119.2, 111.8, 109.1 (br d, J = 17.6), 108.5, 108.3 (minor diastereomer), 81.6 (d, J = 7.3 Hz), 77.3, 72.0, 70.9 (br s), 65.7, 65.2, 64.9 (minor diastereomer), 60.3, 60.1 (minor diastereomer), 48.0 (br s), 39.6, 36.7, 36.3 (minor diastereomer), 36.1, 34.9 (minor diastereomer), 34.7, 34.0, 33.9 (minor diastereomer), 30.5, 30.2 (minor diastereomer), 29.7 (minor diastereomer), 26.9, 26.4, 25.4, 25.0 (br s), 24.1 (br s), 19.5, 19.4 (minor diastereomer), several minor diastereomer peaks overlapping or not observed; LRMS (ESI): RT = 13.1 mins (diode array), calcd for C38H43F3IN3O7Na [M + Na]+: 860.20, found: 860.15; HRMS (ESI) calcd for $C_{38}H_{43}F_3IN_3O_7Na$ $[M + Na]^+$: 860.1995, found: 860.1975

REFERENCES

1. Byrne, A. T. *et al.* Interrogating open issues in cancer precision medicine with patient-derived xenografts. *Nature Reviews Cancer* (2017). doi:10.1038/nrc.2016.140

2. Arnedos, M. *et al.* Precision medicine for metastatic breast cancer-limitations and solutions. *Nature Reviews Clinical Oncology* (2015). doi:10.1038/nrclinonc.2015.123

3. Livingstone, E., Zimmer, L., Vaubel, J. & Schadendorf, D. BRAF, MEK and KIT inhibitors for melanoma: Adverse events and their management. *Chinese Clinical Oncology* (2014). doi:10.3978/j.issn.2304-3865.2014.03.03

4. Spangler, B. *et al.* A Novel Tumor-Activated Prodrug Strategy Targeting Ferrous Iron Is Effective in Multiple Preclinical Cancer Models. *J. Med. Chem.* **59**, 11161–11170 (2016).

5. Torti, S. V & Torti, F. M. Iron and cancer: more ore to be mined. *Nat Rev Cancer* **13**, 342–355 (2013).

6. Manz, D. H., Blanchette, N. L., Paul, B. T., Torti, F. M. & Torti, S. V. Iron and cancer: recent insights. *Ann. N. Y. Acad. Sci.* n/a-n/a (2016). doi:10.1111/nyas.13008

7. Collisson, E. A. *et al.* A Central role for RAF→MEK→ERK signaling in the genesis of pancreatic ductal adenocarcinoma. *Cancer Discov.* (2012). doi:10.1158/2159-8290.CD-11-0347

8. Liu, J. *et al.* Critical role of oncogenic KRAS in pancreatic cancer (Review). *Mol. Med. Rep.* (2016). doi:10.3892/mmr.2016.5196

9. Hirayama, T. *et al.* A universal fluorogenic switch for Fe(II) ion based on N-oxide chemistry permits the visualization of intracellular redox equilibrium shift towards labile iron in hypoxic tumor cells. *Chem. Sci.* (2017). doi:10.1039/c6sc05457a

10. Spangler, B. *et al.* A reactivity-based probe of the intracellular labile ferrous iron pool. *Nat. Chem. Biol.* (2016). doi:10.1038/nchembio.2116

11. Mahajan, S. S. *et al.* A Fragmenting Hybrid Approach for Targeted Delivery of Multiple Therapeutic Agents to the Malaria Parasite. *ChemMedChem* (2011). doi:10.1002/cmdc.201100002

12. Deu, E. *et al.* Ferrous iron-dependent drug delivery enables controlled and selective release of therapeutic agents in vivo. *Proc. Natl. Acad. Sci. U. S. A.* (2013). doi:10.1073/pnas.1312782110

13. Johnson, B. L. *et al.* Desmoplasia and oncogene driven acinar-toductal metaplasia are concurrent events during acinar cell-derived pancreatic cancer initiation in young adult mice. *PLoS One* (2019). doi:10.1371/journal.pone.0221810

14. Mathew, G. *et al.* Targeting of Ras-mediated FGF signaling suppresses Pten-deficient skin tumor. *Proc. Natl. Acad. Sci. U. S. A.* (2016). doi:10.1073/pnas.1604450113

15. Kobayashi, S., Xu, P., Endo, T., Ueno, M. & Kitanosono, T. Chiral copper(II)-

catalyzed enantioselective boron conjugate additions to α,β-unsaturated carbonyl compounds in water. *Angew. Chemie - Int. Ed.* (2012). doi:10.1002/anie.201207343

Chapter 4: Towards the development of Fe(II)-activated prodrugs of histone deacetylase inhibitors as selective anti-myeloma agents

Muir, R.K., Blank, B.R., Steri, V., Hann, B., Renslo, A.R.

INTRODUCTION

Histone deacetylase (HDAC) inhibitors are a class of chemotherapeutics that target the DNA regulation pathways in cancer. There are several classes of HDACi approved as either monotherapy or in combination therapies as anticancer agents.[1] Despite structural differences, HDAC inhibitors share a wide array of toxicities in the clinic, namely thrombocytopenia, neutropenia, fatigue, nausea and cardia arrythmia[2,3] Subsequent work to reduce toxicity revolved primarily around developing isoform-specific HDAC inhibitors, however these molecules shared the same toxicities seen by pan-HDAC inhibitors. This indicates that the toxicity seen is due to on-target, yet off-tissue inhibition and may be mitigated by tissue-specific delivery of these agents.

To address this problem, a few HDAC inhibitor prodrugs have reported, yet only one has reported any results from preclinical models.[4,5] Slusher et al reported an ester-based prodrug approach to improve oral absorption and observed complete conversion to the free hydroxamic acid in mouse plasma within an hour.[6] Recently, the Renslo ab has described a method for Fe(II)-sensitive caging the hydroxamate-containing LpxC inhibitor that showed promising *in vivo* efficacy against an acute *P. aeruginosa* infection model.[7] Here is described the progress towards utilizing the same caging method on Panobinostat as a method to cage known clinical toxicities while maintaining its antimyeloma activity in preclinical models.

RESULTS AND DISCUSSION

Synthesis of TRX-PANO

To access the TRX-PANO scaffold, we attempted to utilize the same coupling scheme that was used to make another trioxolane-caged hydroxamate TRX-LpxC. Panobinostat acid **7** was synthesized as previously described,[7] however the primary products observed were the result of polymerization reactions. A variety of protecting group strategies were attempted, with nosyl selected due to it providing the most efficient deprotection after the coupling reaction.

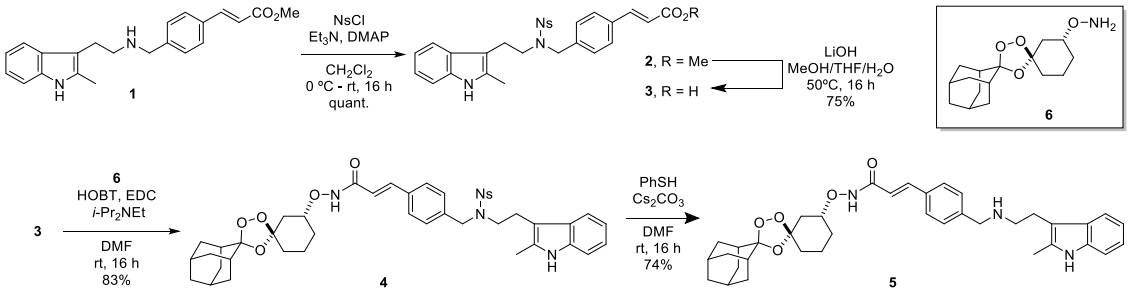

Scheme 4-1: Panobinostat methyl ester **1** was protected with nosyl chloride to give ester **2**. Following saponification, nosyl-protected panobinostat acid **3** was coupled with TRX-Hydroxylamine **6** via EDC/HOBT to give nosyl-TRX-PANO **4**. Deprotection via thiophenol under basic conditions yielded TRX-PANO **5**.

Cellular activity of TRX-PANO in Multiple Myeloma lines

TRX-PANO was then tested for antimyeloma activity in relation to parent Panobinostat in three multiple myeloma lines. TRX-PANO shows dose-dependent cytotoxicity similar to Panobinostat, yet in all three cells the EC_{50} is shifted 5-8 fold less potent (Fig 4-1A). This is consistent with previously reported TRX-based prodrugs and is assumed to be

due to the variation in the concentration of the LIP in these cells.[8,9] To confirm this activity was due to uncaging and subsequent on-target inhibition of HDACs, cells were exposed to either 100 nM of TRX-PANO or PANO and an accumulation of acetylated-H4 was observed after 24 h (Fig 4-1B). This accumulation of acetylated-H4 occurs in a dose-dependent fashion in MM.1S cells after 24 h of dosing indicating sufficient uncaging and subsequent on-target activity.

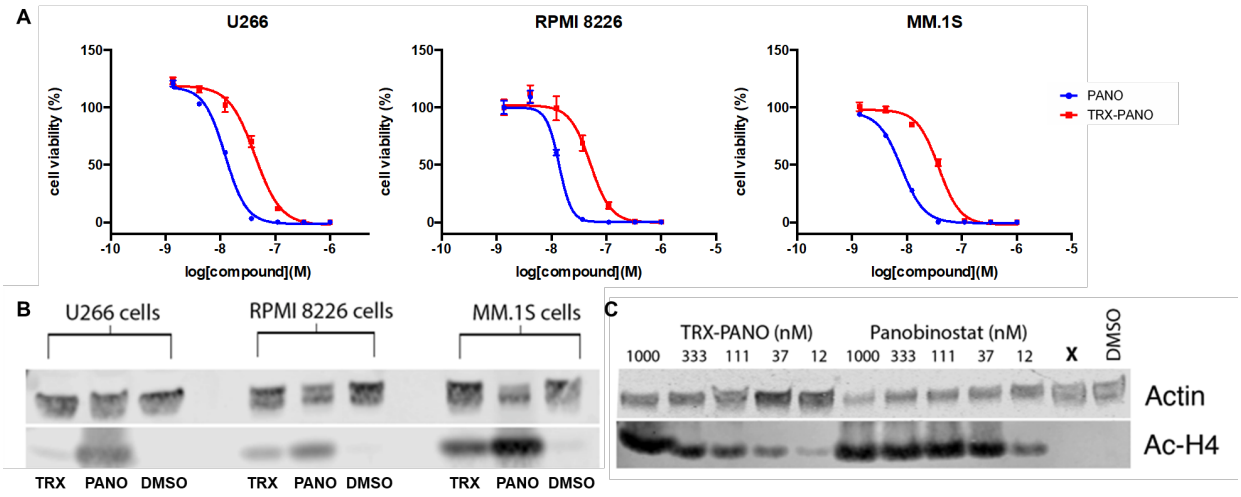

Figure 4-1 **a)** Multiple myeloma cell lines were treated with TRX-Pano or Panobinostat for 72 hours. Cytotoxicity was measured via CellTiter Glo. While TRX-Pano does show a shift in potency, it is still a highly cytotoxic compound to these cells. **B)** To ensure for on-target inhibition, cells were treated with either 100 nM PANO, TRX-PANO or DMSO for 24 hours. At this point, HDAC inhibition was measured by Western blot for acetylated H4. **C)** MM.1S cells were treated with TRX-PANO or PANO for 24 hours. A dose-dependent inhibition of HDACs is observed though potency appears to be less as seen in the cytotoxicity assay

TRX-PANO faces issues *in vivo* due to metabolic instability in mice

With promising cellular data, pharmacokinetic properties of TRX-PANO in NSG mice were determined (Figure 4-3C). However over 24 hours, no TRX-PANO was observed in the plasma of these mice. Instead a typical plasma concentration curve was observed

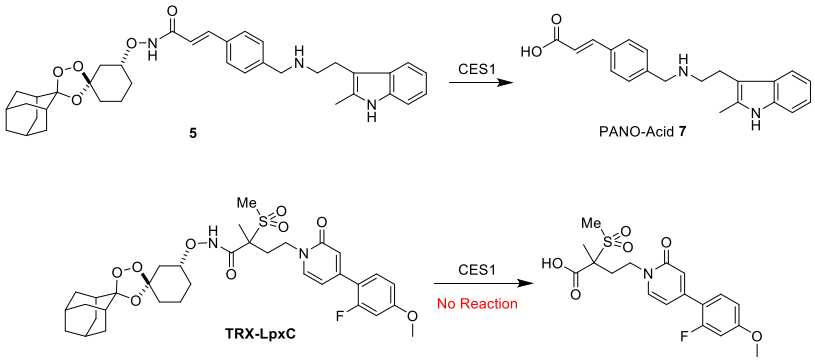

Figure 4-2: TRX-PANO is readily hydrolyzed by CES1 found in abundance in mouse plasma. This is in stark contrast to TRX-LpxC stability

of a hydrolyzed product, PANO-Acid **7**, indicating the parent TRX-PANO to be a substrate for a hydrolase. This data is in direct opposition to the stability of previously reported TRX-caged hydroxamate, TRX-LpxC (Figure 4-2). The instability of TRX-PANO combined with the lack of preclinical data of other non-branching hydroxamate-based prodrugs suggests that hydroxamate esters lacking a quaternary center at the alpha-position are intrinsically unstable due to one or more hydrolases found *in vivo*.

Fortunately at the same time as the mouse PK studies, we also conducted a human plasma stability assay (Figure 4-3A). Confusingly, we found that TRX-PANO is entirely stable in human plasma up to six hours. This lead us to perform a literature review on hydrolases found in mice that are not present, or are present at significantly lower levels in humans, leading us to the esterase CES1c.[10] This esterase is known to be extremely promiscuous, and importantly is found at highly elevated levels in mouse plasma while being virtually nonexistent in human plasma. A plasma stability assay was then performed with TRX-PANO in mouse plasma from wild type Black6 mice (WT) as well as those with plasma CES1 knocked out (CES1 KO). Pleasingly, TRX-PANO has a

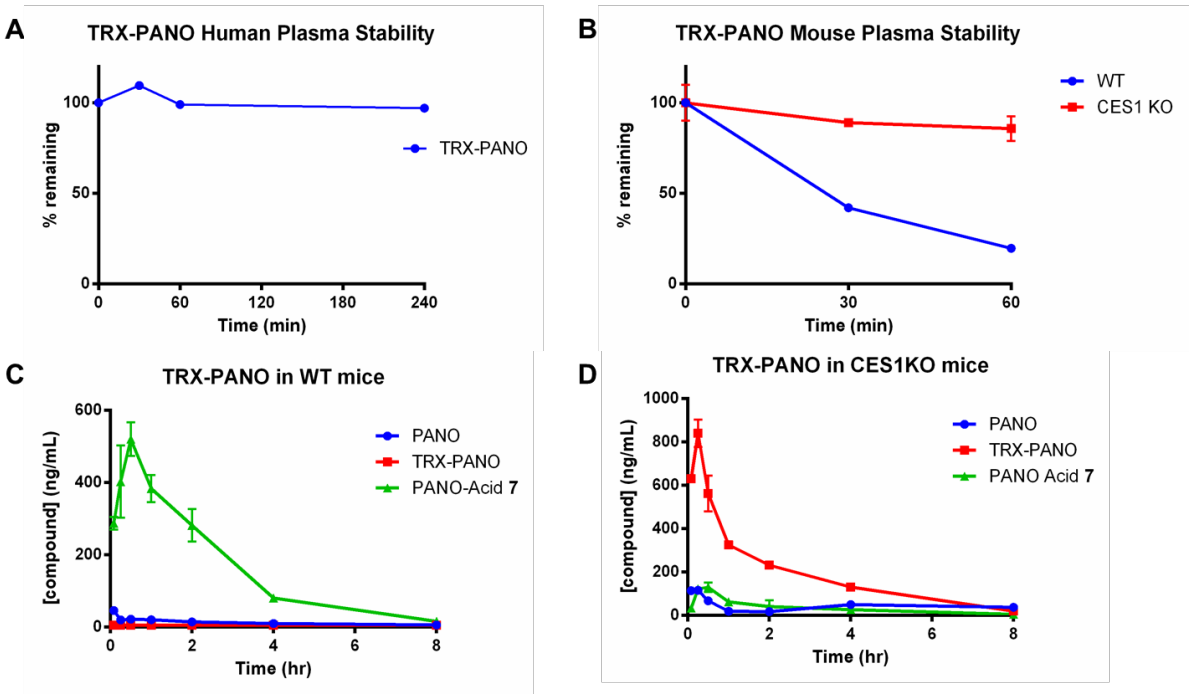

Figure 4-3 **a)** Stability of TRX-PANO in human plasma. **b)** TRX-PANO is significantly more stable in CES1 KO mouse plasma than wild type. **c-d)** Mice were injected with a single dose of TRX-PANO (15 mpk, IP). Plasma was collected at indicated times and plasma drug concentration was determined by LCMS/MS assay (IAS, Berkeley). TRX-PANO is unstable in NSG mice and is observed to be significantly more stable in CES1 KO mice.

significantly prolonged half-life in CES1 KO mice compared to WT, indicating the esterase CES1 as the primary mechanism of instability in NSG mice (Figure 4-3B). A pharmacokinetic assay was then performed in CES1 KO mice which showed significantly improved pharmacokinetic parameters compared to wild type (Figure 3d).

Initial *in vivo* efficacy of TRX-PANO appears encouraging

Unfortunately, the CES1 KO mice used for pharmacokinetic studies were of a Black6 background and were therefore unsuitable for xenograft studies with the human cancer cell lines of interest. Several mouse cancer cell lines were obtained to test for xenograft candidates, however Panobinostat proved to be at minimum two orders of magnitude

less efficacious in all mouse lines than in human multiple myeloma lines. At this point, a paper was published describing the generation of a NOD-SCID CES1 KO mouse line.[11] Two females and one male were purchased from Synthon Biopharmaceuticals and plasma CES1c KO was confirmed by DNA gel (data not shown). To assess this strain's ability to bear a human multiple myeloma xenograft, both NSG and CES1KO NOD-SCID mice were injected with 10^6 cells of MM.1S cells. While MM.1S.luc cells rapidly expands in NSG mice (observed by increased luminescence), the xenograft failed to take in CES1KO NOD-SCID mice (Figure 4-4A). While multiple myeloma is the

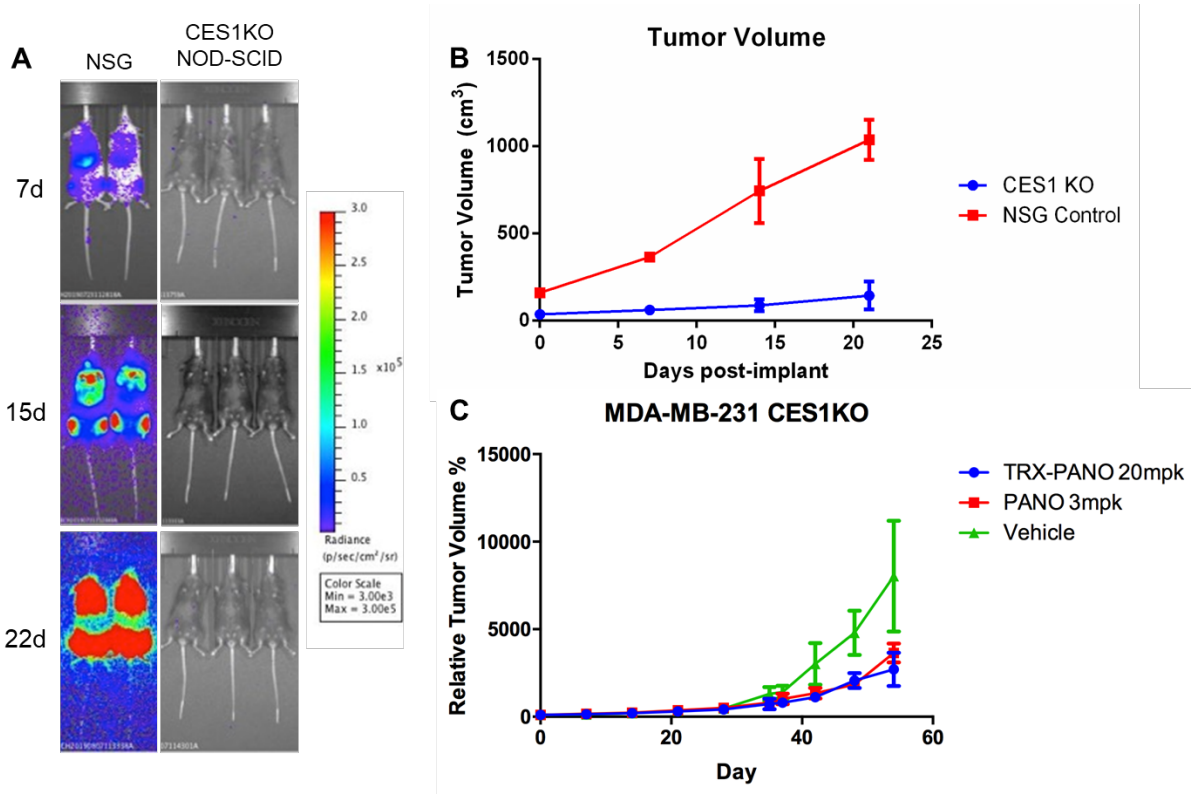

Figure 4-4: **a)** NSG and CES1KO NOD-SCID mice were implanted with 10^x MM.1S.luc cells. After 22 days, no luminescence is seen in NOD-SCID mice indicating a lack of xenograft. **b)** Mice were implanted with MDA-MB-231 cancer cells. Again, it appears xenografts do not grow well in CES1KO NOD-SCID mice.**c)** CES1KO mice bearing MDA-MB-231 xenograft tumors were dosed with TRX-PANO (20mpk), PANO (3mpk) or vehicle (n=2 for each arm) beginning on day 21.

preferred model system as it is the indication Panobinostat is approved for, there is literature suggesting it has significant activity against triple negative breast cancer.[12] The antiproliferative activity of Panobinostat and TRX-PANO were confirmed in MDA-MB-231 cells (data not shown). This triple negative breast cancer cell line was able to expand in the NOD-SCID mice, albeit significantly less than in NSG mice (Figure 4-4B). These mice (n=2) were then dosed with TRX-PANO, Panobinostat, or vehicle for four weeks. While it appears both TRX-PANO and Panobinostat provide anti-tumor activity, the sample size prevents any meaningful conclusions to be drawn from this experiment.

CONCLUSIONS AND FUTURE DIRECTIONS

Future Directions

There are two major future directions for this project: 1) improve the *in vivo* experiments by increasing sample size and/or solving the MM.1S xenograft issue. 2) Perform *in vitro* experiments to prove TRX-PANO cages known off-target toxicities of Panobinostat.

Improving *in vivo* experiments

While the preliminary results are somewhat encouraging, there is significant room for improvement in the future. Firstly, meaningful conclusions cannot be drawn from a sample size of two. This can be remedied by repeating the experiment with more mice, however this has proven difficult due to the problems faced with breeding (slow breeding time, small litter size) leading to not having enough females for breast cancer xenografts. A more appealing solution is to solve the issues with the MM.1S.luc xenograft experiments as it is sex-agnostic. One hypothesis is that because NOD-SCID mice have intact NK cells, the injected cells were primarily killed by the immune system

and therefore did not expand. A simple experiment is a dose-escalation of increasing concentrations of cancer cells.

Demonstrating caged toxicity *in vitro*

Other than simple bodyweight measurements, the clinical toxicities of Panobinostat do not manifest in *in vivo* experiments until testing in rats or dogs. As our lab only has access to mice, this limits our ability to show meaningful caging of the off-targets of Panobinostat. One side effect observed in the clinic is a drop in non-red blood cell counts.[2] To determine if TRX-PANO shows caged activity against this target, PBMCs were treated in dose response with both TRX-PANO and Panobinostat for 72 hours. However, it was determined that neither TRX-PANO nor parent Panobinostat have cytotoxic activity against these cell types *in vitro* (Figure S4-2).

Moving forward, there are two *in vitro* toxicity assays for which Panobinostat reportedly failed in its IND form: the Ames test and the COMET assay.(cite) The COMET assay tests if a compound causes DNA fragmentation in cell culture while the Ames test determines if a compound is mutagenic in the *S.Typhimurium* strain TA97a. A potential difficulty of these assays is both systems are known to have sufficient Fe(II) to uncage trioxolane-based prodrugs, though to varying degrees. A key inclusion for these experiments is to incubate the system with DFO or other iron chelator to minimize TRX uncaging.

MATERIALS AND METHODS

Cell Line and Cell Culture

MM.1S, RPMI 8226 and U266 cells were maintained in an atmosphere of 5% CO2 in RPMI 1640 media purchased from HyClone supplemented with 10% FBS (Gibco) and Pen/Strep (1× final concentration, Gemini BioProducts).

In vitro inhibition

In vitro inhibition was determined using the HDAC-Glo I/II screening system (Promega). Compounds were dissolved in DMSO then diluted in buffer to give a final concentration of 0.1% DMSO. Signal was read using the Flexstation 3 (Molecular Devices)

Western Blots

Cells were plated in 6-well plate at 10^6 cells per well and incubated for at least 24 h prior to exposure to compounds. Cells were then treated with specified concentrations of compound that resulted in a final concentration of 0.1% DMSO. After the specified amount of time, cells were pelleted by centrifuging at 200 x g for 5 minutes. Cell pellets were washed with PBS and then lysed with mPER lysis buffer (Thermo Fisher) containing protease inhibitor cocktail (1x concentration, Sigma). Protein concentration was determined using Pierce BCA assay (Thermo Fisher). Samples were normalized to 20 µg per well and run on a 4-12% Bis-Tris Protein Gel (Thermo Fisher). Transfer and blotting was performed using the iBlot 2 and iBind system (Thermo Fisher)

Cell toxicity assay

Cells were plated in 96-well Greiner black μClear tissue culture plates at 10^4 cells per well for at least 24 h prior to exposure to compounds. Cells were then treated in triplicate with escalating concentrations of compound performed in media containing a final concentration of 0.1% DMSO and 200 μL of media per well. Cell viabilities were determined 72 h after treatment by Cell-Titer Glo assay (Promega) on the Flexstation 3 reader (Molecular Devices). Relative luminescent units (RLU) were plotted against corresponding drug concentrations and fitted with a standard four-parameter sigmoidal curve with GraphPad Prism 6. Data reported at the IC_{50}, and error bars represent SEM.

Plasma Stability Assay

CES1 KO Black6 mouse plasma was graciously gifted from Dr. Barbara Slusher (John's Hopkins, MD). To mouse plasma warmed to 37°C was added TRX-PANO in DMSO to give a final concentration of 10 μM with 0.1% DMSO. Aliquots were taken at 0, 30 & 60 minutes and immediately extracted with acetonitrile. The organic layers were collected and compound concentration were determined by mass spectrometry.

Pharmacokinetic Assays

NSG, CES1KO Black6, or CES1KO NOD-SCID mice were administered a single IP dose of TRX-PANO (17.5 mpk, n=3). Blood was collected at indicated timepoints and

from which drug concentrations were determined by Integrated Analytical Solutions, Inc (Berkeley, CA).

Mouse efficacy

Mice were implanted with 10^6 MDA-MB-231 cells. Once tumor volumes reached approximately 100 cm^3, mice were administered IP doses of TRX-PANO (20 mpk), Panobinostat (3 mpk), or vehicle three days per week for four weeks. Efficacy was measured by monitoring tumor volume.

Mouse Genotyping

Tails were collected from three CES1 KO NOD-SCID mice purchased from Synthon Biopharmaceuticals. DNA was extracted by boiling in 25 mM NaOH and 0.2 mM EDTA. The pH of this solution was adjusted to 5.5 by addition of 40 mM Tris HCl (pH 5.5) and the resulting solution was centrifuged at 4000 rpm for 3 minutes. PCR was performed on the supernatant followed by gel electrophoresis to confirm complete CES1 knockout.

Other

Graphing and analysis of data were done using GraphPad Prism 6 software and Microsoft Excel 2010. Figures were prepared with Adobe Design Standard CS6 software.

SUPPORTING INFORMATION

Supplemental Figures

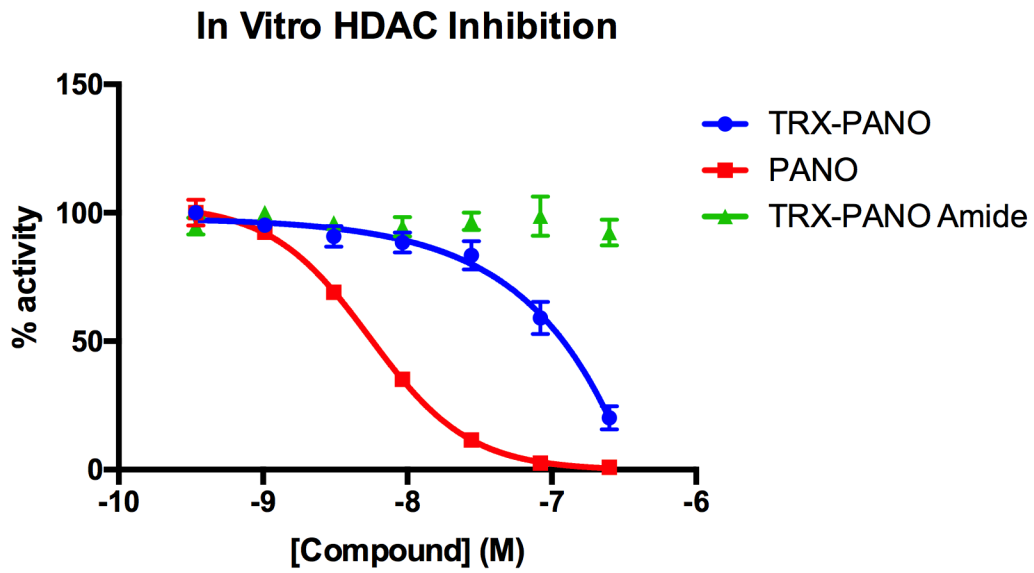

Figure S4-1: In Vitro HDAC inhibition of HeLa nuclear extract. Panobinostat IC_{50} was consistent with literature values (5.5 nM). TRX-PANO showed reduced yet not fully masked activity in the in vitro setting (~125 μM).

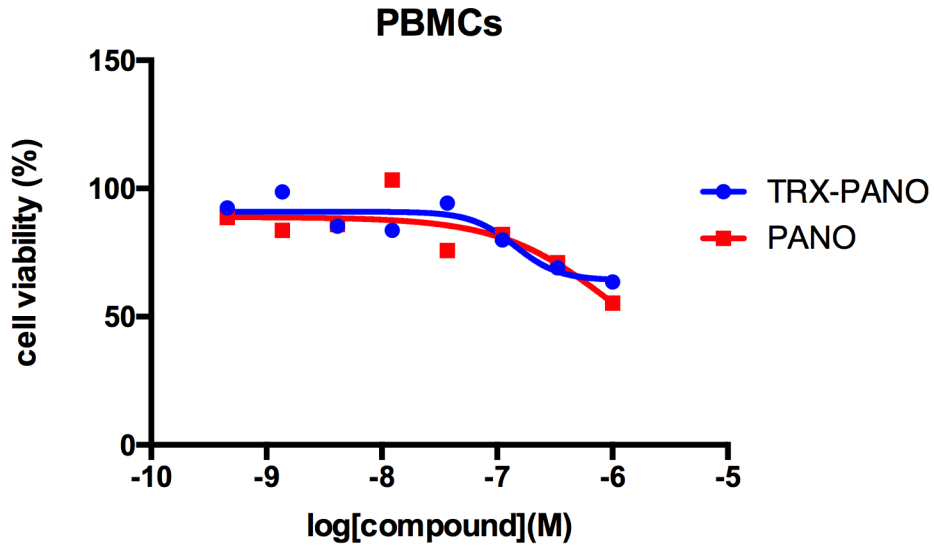

Figure S4-2: Cell viability of PBMCs after 72 hours of treatment. Panobinostat and TRX-PANO show negligible toxicity.

Synthesis

Compound **1** (methyl(2E)-3-[4-({[2-(2-methyl-1H-indol-3-yl)ethyl]amino}methyl)phenyl]prop-2-enoate) was synthesized as described in WO2007/21682. 2007, A1

Compounds **6** (*O*-(dispiro[adamantane-2,3'-[1,2,4]trioxolane-5',1''-cyclohexan]-3''-yl)hydroxylamine) was synthesized as previously described (ACS Inf Disease)

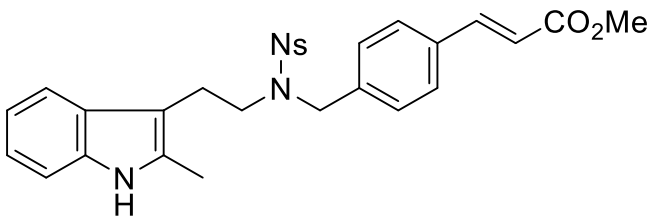

methyl (2E)-3-[4-({N-[2-(2-methyl-1H-indol-3-yl)ethyl]4-nitrobenzenesulfonamido}methyl)phenyl]prop-2-enoate (2). To a round bottom flask equipped with an argon inlet adapter, stirbar, and rubber septum was charged a solution of **1** (2.78g, 7.98 mmol, 1 equiv.) in dichloromethane (80 mL). This solution was cooled to 0°C, at which point triethylamine (1.67mL, 11.98 mmol, 1.5 equiv.), 4-dimethylaminopyridine (97.5mg, 0.80 mmol, 0.1 equiv.) and 4-nitrobenzenesulfonyl chloride (1.95g, 8.77 mmol, 1.1 equiv.) were added sequentially. This cloudy orange mixture was allowed to warm to room temperature overnight then organic solvent was removed under vacuum to give an orange solid. This was then dissolved in 200 mL of EtOAc and washed with two 100 mL portions of satd. aq. $NaHCO_3$ each. The aqueous

layer was then extracted with two 100 mL portions of EtOAc. Organic layers were combined and washed with one 100 mL portion of satd. aq NaCl, dried over $MgSO_4$, filtered and solvent removed under vacuum to afford **methyl (2E)-3-[4-({N-[2-(2-methyl-1H-indol-3-yl)ethyl]4-nitrobenzenesulfonamido}methyl)phenyl]prop-2-enoate** (4.25g, quant.) as a bright orange solid. MS (ESI) calculated for $C_{28}H_{27}N_3O_6S$ $[M + H]^+$ *m/z* 534.17, found 534.08.

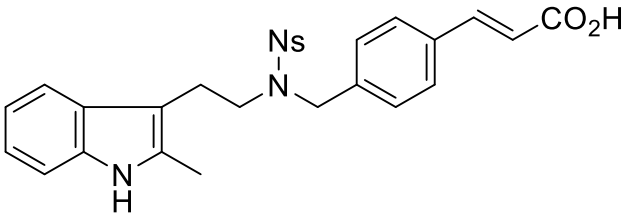

(2E)-3-[4-({N-[2-(2-methyl-1H-indol-3-yl)ethyl]4-nitrobenzenesulfonamido}methyl)phenyl]prop-2-enoic acid (3). To a round bottom flask equipped with an argon inlet adapter, stirbar, and rubber septum was charged a solution of **2** (4.25g, 7.98 mmol, 1 equiv.) in THF (50 mL) and MeOH (50 mL). To this suspension was added 1M LiOH in water (50 mL, 47.9 mmol, 6 equiv,). This suspension was then stirred at 50°C for 16 hours at which point organic solvent was removed under vacuum. This was then dissolved in 200 mL of EtOAc and 50 mL of water and cooled to 0°C before adjusting the pH to 1 through addition of 10% aq. HCl. The organic layer was collected and washed with two 50 mL portions of 1M aq. HCl. The aqueous layer was then extracted with two 500 mL portions of EtOAc. Organic layers were combined and washed with one 100 mL portion of satd. aq NaCl, dried over $MgSO_4$, filtered and solvent removed under vacuum to afford **(2E)-3-[4-({N-[2-(2-methyl-1H-indol-3-**

yl)ethyl]4-nitrobenzenesulfonamido}methyl)phenyl]prop-2-enoic acid (4.13g, 97%) as a bright orange solid. 1H NMR (400 MHz, DMF-d_7) δ ppm 2.32 - 2.43 (m, 3 H) 3.02 - 3.08 (m, 3 H) 3.43 - 3.58 (m, 3 H) 4.82 (s, 2 H) 6.79 (d, J=16.07 Hz, 1 H) 7.00 - 7.12 (m, 2 H) 7.29 - 7.39 (m, 2 H) 7.68 (d, 2 H) 7.77 - 7.89 (m, 1 H) 7.92 (m, 2 H) 8.22 - 8.31 (m, 2 H) 8.50 - 8.56 (m, 2 H) 10.80 (s, 1 H). MS (ESI) calculated for $C_{27}H_{25}N_3O_6S$ $[M + H]^+$ *m/z* 520.15, found 520.09.

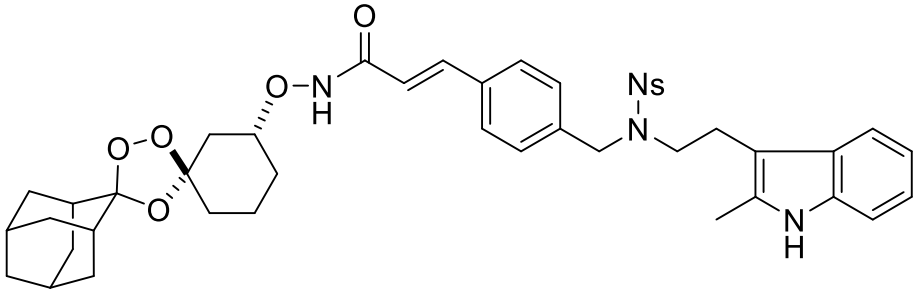

(2E)-N-{dispiro[adamantane-2,2'-[1,2,4]trioxolane-4',1''-cyclohexan]-3''-yloxy}-3-[4-({N-[2-(2-methyl-1H-indol-3-yl)ethyl]4-nitrobenzenesulfonamido}methyl)phenyl]prop-2-enamide (4). To a round bottom flask equipped with an argon inlet adapter, stir bar, and rubber septum was charged a solution of **6** (113.3mg, 0.38 mmol, 1 equiv.) in DMF (8 mL) and a solution of **3** (230mg, 0.44 mmol, 1.15 equiv.) in DMF (8 mL). To this solution was added 1-hydroxybenzotriazole hydrate (68mg, 0.50 mmol, 1.3 equiv.), *N*,*N*-diisopropylethylamine (0.08 mL, 1.01 mmol, 2.6 equiv.) then *N*-(3-dimethylaminopropyl)-*N'*-ethylcarbodiimide hydrochloride (96mg, 0.50 mmol, 1.3 equiv.) sequentially. This deep orange solution stirred at rt for 16 hours at which point the reaction was diluted with 50 mL of EtOAc and 50 mL of satd. aq. $NaHCO_3$.The organic layer was collected and washed with two 50

mL portions of satd. aq. $NaHCO_3$. The aqueous layers were then combined and extracted with two 50 mL portions of EtOAc. Organic layers were combined and washed with one 50 mL portion of satd. aq NaCl, dried over $MgSO_4$, filtered and solvent removed under vacuum to afford an orange oil. The residue was then purified through flash column chromatography (0-40% EtOAc/Hexanes) to yield **(2E)-N-{dispiro[adamantane-2,2'-[1,2,4]trioxolane-4',1''-cyclohexan]-3''-yloxy}-3-[4-({N-[2-(2-methyl-1H-indol-3-yl)ethyl]4-nitrobenzenesulfonamido}methyl)phenyl]prop-2-enamide** (226mg, 74%). 1H NMR (400 MHz, DICHLOROMETHANE-d2) δ ppm 1.23 - 1.48 (m, 3 H) 1.64 - 1.89 (m, 12 H) 1.89 - 2.02 (m, 4 H) 2.06 - 2.22 (m, 3 H) 2.26 - 2.41 (m, 1 H) 2.68 - 2.80 (m, 2 H) 3.23 - 3.36 (m, 2 H) 3.97 (s, 1 H) 4.41 - 4.50 (m, 2 H) 6.92 - 7.04 (m, 2 H) 7.14 (d, 2 H) 7.28 - 7.46 (m, 2 H) 7.46 - 7.54 (m, 2 H) 7.54 - 7.74 (m, 1 H) 7.85 (d, 2 H) 7.94 - 8.10 (m, 1 H) 8.17 (d, 2 H)). 13C NMR (100 MHz, DICHLOROMETHANE-d2) δ ppm 11.71, 20.17, 24.31, 27.11, 27.50, 29.84, 34.34, 35.24, 35.33, 36.88, 36.98, 37.17, 39.49, 48.64, 52.31, 54.39, 107.86, 109.45, 110.85, 112.18, 117.81, 119.70, 121.50, 124.66, 128.45, 129.55, 132.42, 135.70, 146.04, 150.23. MS (ESI) calculated for $C_{43}H_{48}N_4O_8S$ $[M - H]^-$ *m/z* 795.31, found 795.56.

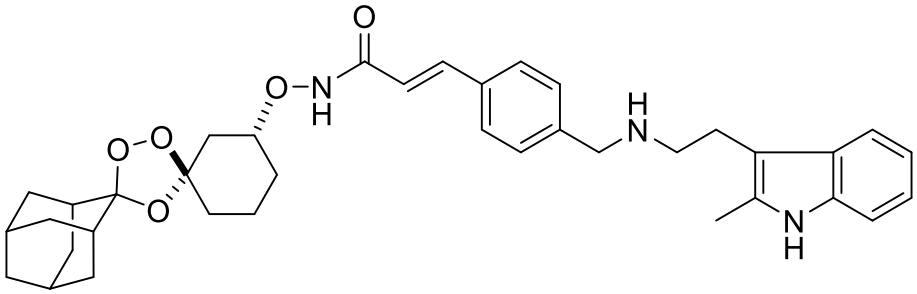

(2E)-N-{dispiro[adamantane-2,2'-[1,2,4]trioxolane-4',1''-cyclohexan]-3''-yloxy}-3-[4-({N-[2-(2-methyl-1H-indol-3-yl)ethyl]amino}methyl)phenyl]prop-2-enamide (5, TRX-PANO). To a round bottom flask equipped with an argon inlet adapter, stirbar, and rubber septum was charged a solution of **4** (207mg, 0.26 mmol, 1 equiv.) in DMF (12 mL). To this solution was added $CsCO_3$ (507mg, 1.55 mmol, 6 equiv,) and thiophenol (0.106mL, 1.04 mmol, 4 equiv.). This suspension was then stirred at rt for 16 hours at which point the reaction was diluted with 50 mL of EtOAc, 30 mL of satd. aq $NaHCO_3$ and 20 mL of water. The organic layer was separated and washed with two 50 mL portions of satd. aq $NaHCO_3$. The aqueous layers were combined and extracted with two 50 mL portions of EtOAc. Organic layers were combined and washed with one 100 mL portion of satd. aq NaCl, dried over $MgSO_4$, filtered and solvent removed under vacuum to afford a yellow oil. The residue was then purified through flash column chromatography (0-10% MeOH/CH2CL2) to yield **(2E)-N-{dispiro[adamantane-2,2'-[1,2,4]trioxolane-4',1''-cyclohexan]-3''-yloxy}-3-[4-({N-[2-(2-methyl-1H-indol-3-yl)ethyl]amino}methyl)phenyl]prop-2-enamide** (117mg, 74%). 1H NMR (400 MHz, METHANOL-d4) δ ppm 1.19 - 1.42 (m, 3 H) 1.55 - 1.82 (m, 13 H) 1.82 - 2.02 (m, 7 H) 2.06 - 2.13 (m, 1 H) 2.32 (s, 3 H) 2.36 - 2.43 (m, 1 H) 2.77 - 2.87 (m, 2 H) 2.87 - 2.97 (m, 2 H) 3.76 (s, 2 H) 3.82 - 3.94 (m, 1 H) 6.43 (d, J=15.71 Hz, 1 H) 6.86 - 7.03 (m, 2 H) 7.23 (dd, J=7.97, 4.57 Hz, 3 H) 7.33 - 7.41 (m, 1 H) 7.44 (br d, J=8.04 Hz, 2 H) 7.56 (d, J=15.71 Hz, 1 H). 13C NMR (100 MHz, METHANOL-d4) δ ppm 11.57, 14.61, 20.94, 24.84, 28.03, 28.43, 30.60, 34.99, 35.88, 37.83, 37.88, 37.92, 40.59, 50.27, 53.79, 61.66, 82.88, 108.65, 110.36, 111.53, 112.66, 118.24, 118.53, 119.66, 121.58, 129.19,

129.93, 130.21, 133.32, 135.29, 137.26, 142.00, 142.23, 166.60. MS (ESI) calculated for $C_{37}H_{45}N_3O_5$ $[M + H]^+$ *m/z* 612.34, found 612.23.

References

1. Suraweera, A., O'Byrne, K. J. & Richard, D. J. Combination therapy with histone deacetylase inhibitors (HDACi) for the treatment of cancer: Achieving the full therapeutic potential of HDACi. *Frontiers in Oncology* (2018). doi:10.3389/fonc.2018.00092

2. Subramanian, S., Bates, S. E., Wright, J. J., Espinoza-Delgado, I. & Piekarz, R. L. Clinical toxicities of histone deacetylase inhibitors. *Pharmaceuticals* (2010). doi:10.3390/ph3092751

3. Shen, S. & Kozikowski, A. P. Why Hydroxamates May Not Be the Best Histone Deacetylase Inhibitors--What Some May Have Forgotten or Would Rather Forget? *ChemMedChem* **11**, 15–21 (2016).

4. Liao, Y. *et al.* H2O2/Peroxynitrite-Activated Hydroxamic Acid HDAC Inhibitor Prodrugs Show Antileukemic Activities against AML Cells. *ACS Med. Chem. Lett.* (2018). doi:10.1021/acsmedchemlett.8b00057

5. El Bahhaj, F., Dekker, F. J., Martinet, N. & Bertrand, P. Delivery of epidrugs. *Drug Discovery Today* (2014). doi:10.1016/j.drudis.2014.03.017

6. Rais, R. *et al.* Discovery of a para-Acetoxy-benzyl Ester Prodrug of a Hydroxamate-Based Glutamate Carboxypeptidase II Inhibitor as Oral Therapy for Neuropathic Pain. *J. Med. Chem.* (2017). doi:10.1021/acs.jmedchem.7b00825

7. Blank, B. R. *et al.* Targeting Mobilization of Ferrous Iron in Pseudomonas aeruginosa Infection with an Iron(II)-Caged LpxC Inhibitor. *ACS Infect. Dis.*

(2019). doi:10.1021/acsinfecdis.9b00057

8. Spangler, B. *et al.* A reactivity-based probe of the intracellular labile ferrous iron pool. *Nat. Chem. Biol.* (2016). doi:10.1038/nchembio.2116

9. Spangler, B. *et al.* A Novel Tumor-Activated Prodrug Strategy Targeting Ferrous Iron Is Effective in Multiple Preclinical Cancer Models. *J. Med. Chem.* **59**, 11161–11170 (2016).

10. Bahar, F. G., Ohura, K., Ogihara, T. & Imai, T. Species difference of esterase expression and hydrolase activity in plasma. *J. Pharm. Sci.* (2012). doi:10.1002/jps.23258

11. Ubink, R. *et al.* Unraveling the interaction between carboxylesterase 1C and the antibody-drug conjugate SYD985: Improved translational PK/PD by using Ces1C knockout mice. *Mol. Cancer Ther.* (2018). doi:10.1158/1535-7163.MCT-18-0329

12. Tate, C. R. *et al.* Targeting triple-negative breast cancer cells with the histone deacetylase inhibitor panobinostat. *Breast Cancer Res.* (2012). doi:10.1186/bcr3192

Chapter 5: Future Directions

While this work has suggested a connection between KRAS mutations and an elevated labile iron pool, this by no means tells the complete story. Iron homeostasis is a highly complex and regulated system, and we plan to probe how different genes affect this network. To do so, we propose to perform a TRX-based CRISPRi and CRISPRa screen on various genes thought to be involved in iron metabolism. The system to be used is a Tet-on GFP reporter, in which introduction of tetracycline (or similar analogs) will cause the production of cellular GFP. We first caged doxycycline with the TRX platform so that it may not interact with the Tet-promoter unless reacted first with Fe(II) (Scheme 5-1).

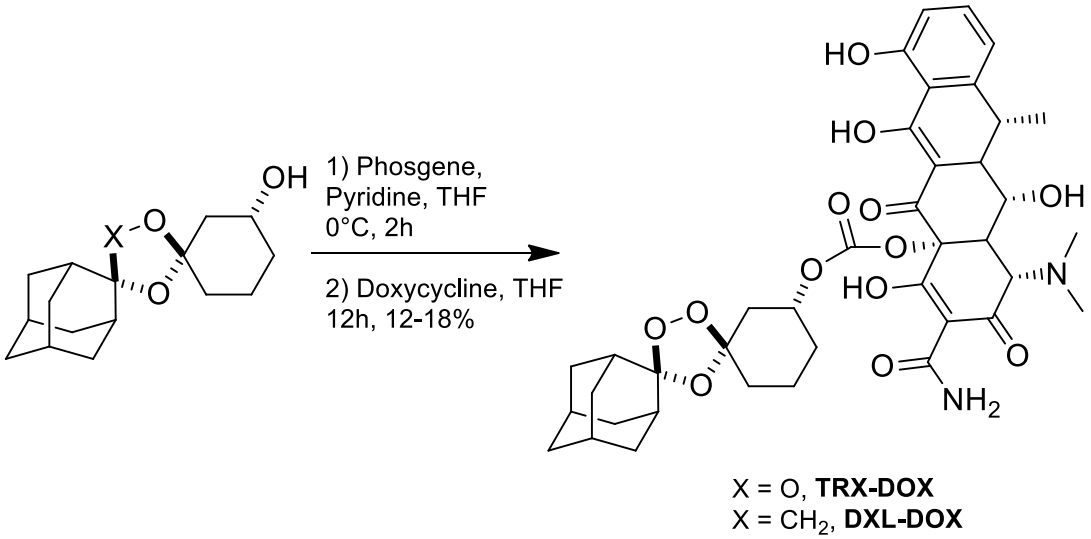

Scheme 5-1**:** Synthesis of TRX-DOX. Racemic TRX or DXL alcohol in pyridine and THF was cooled before activation with phosgene. After 2 hours, the chloroformate was reacted with excess doxycycline to produce TRX- and DXL-DOX. Stereochemistry is based on literature and is currently unconfirmed.

As TRX-DOX is formed through a carbonate linkage as opposed to the traditional carbamate, DXL-DOX was synthesized as well as a control for carbonate stability in cells. Tet-on GFP K562 cells were then dosed with varying concentrations of doxycycline (DOX), TRX-DOX, and DXL-DOX. Pleasingly, cells dosed with DXL-DOX

showed no GFP signal, indicating the carbonate linkage of TRX-DOX both disrupts interaction with the Tet promoter and is stable in these cells (Fig 5-2A). At the same time, TRX-DOX shows a dose-dependent increase in GFP signal consistent with increasing delivery of doxycycline. Importantly, the amount of GFP expressing cells increases upon iron preloading and decreases upon iron withholding (Figure 5-2B,C). These probes along with the Tet-on GFP cells allow us to measure changes in labile iron pool concentrations in a high-throughput CRISPR screen.

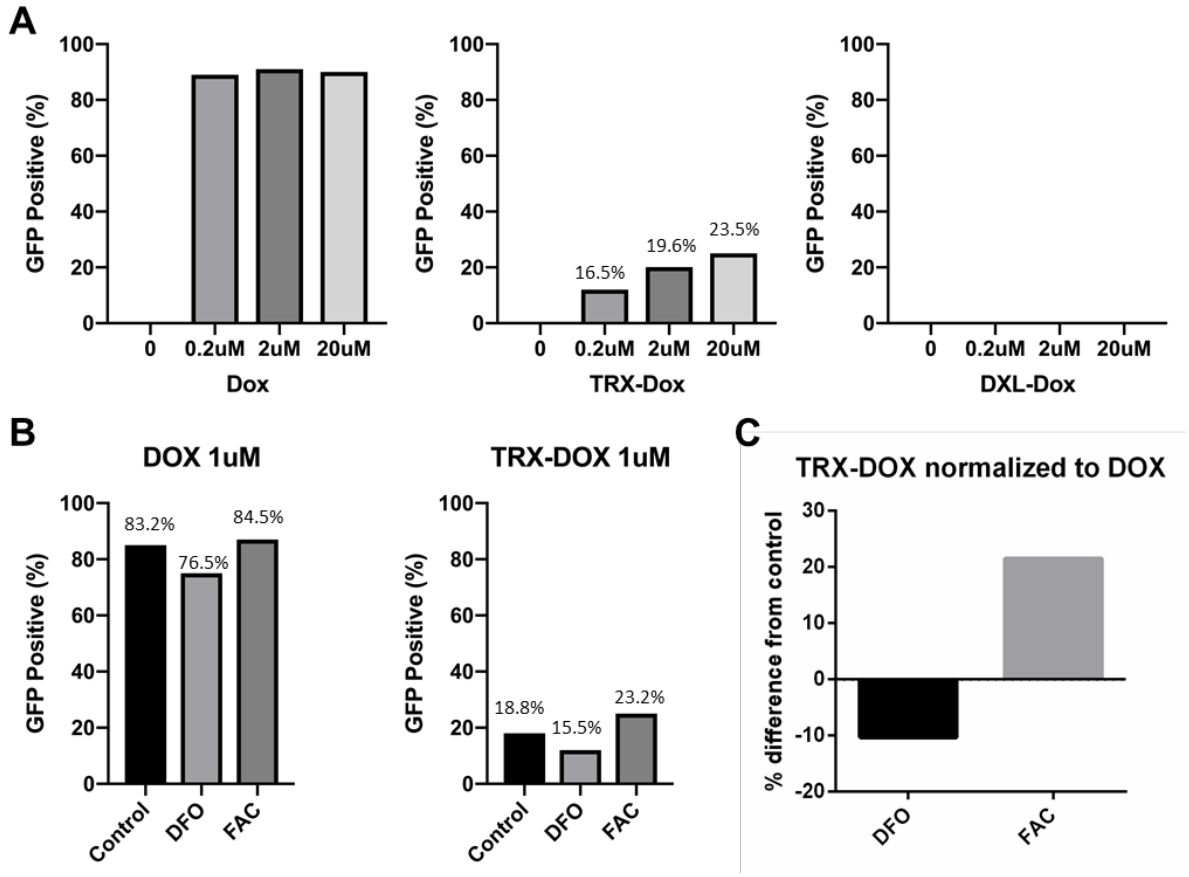

Figure 5-1 **a)** K562 cells with dox-inducible GFP were dosed with Dox, TRX-DOX and DXL-DOX at varying concentrations. TRX-DOX shows dose-dependent activation of GFP while DXL-Dox remains inactive indicating ample caging. **b)** Cells were pretreated with either FAC (500 μM), DFO (300 μM), or DMSO (0.1%) for 2 hours before dosing. DFO appears to reduce GFP signal in both treatments while FAC increases only in TRX-DOX treated cells. **c)** Normalized signal from **B**. TRX-DOX normalized to free DOX. Then, DFO or FAC normalized to cells pretreated with DMSO.

Publishing Agreement

It is the policy of the University to encourage the distribution of all theses, dissertations, and manuscripts. Copies of all UCSF theses, dissertations, and manuscripts will be routed to the library via the Graduate Division. The library will make all theses, dissertations, and manuscripts accessible to the public and will preserve these to the best of their abilities, in perpetuity.

Please sign the following statement:

I hereby grant permission to the Graduate Division of the University of California, San Francisco to release copies of my thesis, dissertation, or manuscript to the Campus Library to provide access and preservation, in whole or in part, in perpetuity.

DocuSigned by:
Ryan Muir
C603831079C7426...

Author Signature

12/18/2019

Date